Calhoun
Institutional Archive of the Naval Postgraduate School

Calhoun: The NPS Institutional Archive

Theses and Dissertations | Thesis Collection

1986-06

An examination of radiation in an integrated marine atmospheric boundary layer model

Dreksler, Steven B.

http://hdl.handle.net/10945/21840

DUDLEY KNOX LIBRARY

http://www.nps.edu/library

Calhoun is a project of the Dudley Knox Library at NPS, furthering the precepts and goals of open government and government transparency. All information contained herein has been approved for release by the NPS Public Affairs Officer.

Dudley Knox Library / Naval Postgraduate School
411 Dyer Road / 1 University Circle
Monterey, California USA 93943

DUDLEY KNOX LIBRARY
NAVAL POSTGRADUATE SCHOOL
MONTEREY CALIFORNIA 93943-5002

NAVAL POSTGRADUATE SCHOOL
Monterey, California

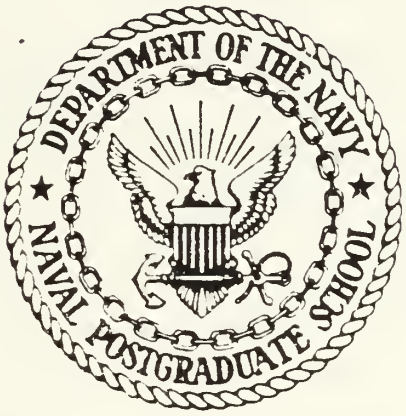

THESIS

An Examination of Radiation in an
Integrated Marine
Atmospheric Boundary Layer Model

by

Steven B. Dreksler

June 1986

Thesis Advisor: K. L. Davidson

Approved for public release; distribution unlimited

T230362

SECURITY CLASSIFICATION OF THIS PAGE

REPORT DOCUMENTATION PAGE

1a REPORT SECURITY CLASSIFICATION	1b. RESTRICTIVE MARKINGS
2a SECURITY CLASSIFICATION AUTHORITY	3 DISTRIBUTION / AVAILABILITY OF REPORT
2b DECLASSIFICATION / DOWNGRADING SCHEDULE	
4 PERFORMING ORGANIZATION REPORT NUMBER(S)	5 MONITORING ORGANIZATION REPORT NUMBER(S)
6a. NAME OF PERFORMING ORGANIZATION / 6b OFFICE SYMBOL *(If applicable)*	7a NAME OF MONITORING ORGANIZATION
6c. ADDRESS *(City, State, and ZIP Code)*	7b. ADDRESS *(City, State, and ZIP Code)*
8a NAME OF FUNDING / SPONSORING ORGANIZATION / 8b OFFICE SYMBOL *(If applicable)*	9 PROCUREMENT INSTRUMENT IDENTIFICATION NUMBER
8c ADDRESS *(City, State, and ZIP Code)*	10 SOURCE OF FUNDING NUMBERS

PROGRAM ELEMENT NO	PROJECT NO	TASK NO	WORK UNIT ACCESSION NO

11 TITLE *(Include Security Classification)*

12 PERSONAL AUTHOR(S)

13a TYPE OF REPORT	13b TIME COVERED FROM _____ TO _____	14 DATE OF REPORT *(Year, Month, Day)*	15 PAGE COUNT

16 SUPPLEMENTARY NOTATION

17 COSATI CODES			18 SUBJECT TERMS *(Continue on reverse if necessary and identify by block number)*
FIELD	GROUP	SUB-GROUP	

19 ABSTRACT *(Continue on reverse if necessary and identify by block number)*

An integrated marine atmospheric boundary layer (MABL) model is evaluated relative to its ability to estimate longwave and shortwave radiation. The model is initialized and verified using data taken during the 1983 Mixed Layer Dynamics Experiment (MILDEX). Model computations of shortwave and longwave radiation are compared with measurements made during both atmospheric frontal and non-frontal situations. The model results did not always agree with the measurements but reasons for them seem to be known and are discussed. One problem is that the MABL model only predicts clouds in the boundary layer and does not consider upper clouds. This led to most of the major differences. Further development of the model with upper-layer cloud specifications is needed to overcome the major differences encountered in this evaluation.

20 DISTRIBUTION / AVAILABILITY OF ABSTRACT ☐ UNCLASSIFIED/UNLIMITED ☐ SAME AS RPT ☐ DTIC USERS	21 ABSTRACT SECURITY CLASSIFICATION	
22a NAME OF RESPONSIBLE INDIVIDUAL	22b TELEPHONE *(Include Area Code)*	22c OFFICE SYMBOL

Approved for public release; distribution is unlimited.

An Examination of Radiation in an Integrated Marine Atmospheric Boundary Layer Model

by

Steven B. Dreksler
Captain, United States Air Force
B.S., University of Maryland, 1977

Submitted in partial fulfillment of the
requirements for the degree of

MASTER OF SCIENCE IN METEOROLOGY

from the

NAVAL POSTGRADUATE SCHOOL
June 1986

ABSTRACT

An integrated marine atmospheric boundary layer (MABL) model is evaluated relative to its ability to estimate longwave and shortwave radiation. The model is initialized and verified using data taken during the 1983 Mixed Layer Dynamics Experiment (MILDEX). Model computations of shortwave and longwave radiation are compared with measurements made during both atmospheric frontal and non-frontal situations. The model results did not always agree with the measurements but reasons for them seem to be known and are discussed. One problem is that the MABL model only predicts clouds in the boundary layer and does not consider upper clouds. This led to most of the major differences. Further development of the model with upper-layer cloud specifications is needed to overcome the major differences encountered in this evaluation.

TABLE OF CONTENTS

LIST OF TABLES

LIST OF FIGURES

ACKNOWLEDGEMENTS

I wish to thank:

- Professor K.L. Davidson for his continuous guidance and assistance in completing this thesis;
- Professor P. A. Durkee for his review of the thesis and constructive criticism;
- Ms. P. J. Boyle for training me on the MABL model and her enormous assistance in data acquisition;
- Ms. S. Fellbaum for diligently retrieving and processing MILDEX data, and supplying me with the synoptic charts and satellite pictures;
- Dr. Kristina Katsaros and Mr. Richard Lind at the Atmospheric Science Deparment at the University of Washington in Seattle for supplying and discussing MILDEX radiation measurements and data;
- Scripps Institute of Oceanography for providing satellite pictures and data from the R/P Flip.

Very special thanks to my wife, Therese Bilodeau for her undoubted patience, understanding, love and support over the last two years, while I worked to earn my degree.

I. INTRODUCTION

Understanding properties of and processes which affect the atmospheric boundary layer is crucial to Department of Defense operations. For example, the performance of nearly all electro-magnetic (EM) and electro-optical (EO) systems is affected by conditions in the marine atmospheric boundary layer (MABL). Signal performance is distorted by refraction, wave front distortion and extinction. Refraction, which leads to the formation of ducts and the trapping of EM signals, is determined by the vertical gradient of the index of refraction, which is a function of the vertical gradients of temperature, humidity and pressure. EO systems are affected by small scale inhomogeneities in the index of refraction (due to turbulence), and by water vapor and aerosol concentrations in the MABL. Extinction is due to water vapor absorption and marine aerosol scattering in the presence of high humidity, and thus is normally restricted to the MABL.

Radiation fluxes coupled with atmospheric dynamics and thermodynamics is recognized as one of the major features of the MABL. Clouds are the most dominant components in affecting the radiation budget of the atmosphere and in modifying heating and cooling features of the surface and at cloud tops.

The height of the MABL is controlled to a large extent by thermal forcing. During the day, heat is added to the surface and is transported upward by buoyant thermal turbulent eddies. The impingement of the stable layer by these eddies entrains overlying air so that in the absence of subsidence, the inversion height will rise as long as there is an upward heat flux at the surface. The turbulence of the cloud topped PBL is also driven by radiational cooling

at the cloud top. Hence, radiational cooling at the top of the mixed layer is effective at producing entrainment.

The purpose of this thesis is to examine the ability to estimate radiation in the boundary layer with a simple MABL model. The model used is a MABL model which has been developed at the Naval Postgraduate School (NPS) (Davidson et al, 1984). This examination was based on the use of simple mixed layer parameterizing of specific humidity and potential temperature, and the use of a simplified boundary layer radiation model. This is in comparison to other schemes which could have been used. These include the use of a simplified radiation scheme with detailed atmospheric description or the use of a detailed radiation model with simple mixed layer parameters for describing the MABL. The scheme chosen may confuse the causes of resulting inaccuracies, since it is not known whether the inaccuracies result from incomplete radiation calculations or from incomplete vertical profiles.

The use of potential temperature and specific humidity within the well-mixed region and their gradients at the base of the inversion also makes this model applicable to studying inversion changes. The model diagnoses time evolutions of the mixed layer values of inversion height, potential temperature and specific humidity, as well as their jumps at the inversion (Davidson et al,1984).

The data used in this study were collected during the Office of Naval Research sponsored Mixed Layer Dynamics Experiment (MILDEX) between 24 October 1983 and 10 November 1983. MILDEX is an offshore experiment designed to collect intensive Ocean Boundary Layer (OBL) and MABL data, for model verification. MILDEX was conducted in the eastern north Pacific Ocean, 150 miles off the coast of Lompoc, California.

A secondary objective of this thesis is to present a thorough description of synoptic features occurring during MILDEX. Therefore, synoptic descriptions beyond that needed for radiation-model considerations are presented in these discussions.

II. MODEL DESCRIPTION

Boundary layer research has led to several time dependent MABL models based on entrainment energetics and radiative fluxes (e.g. Deardorff, 1976; Stage and Businger, 1981; Davidson et al., 1984).

The Naval Postgraduate School (NPS) model (Davidson et al, 1984), used in this thesis, is a zero-order two-layer, integrated mixed-layer model, consisting of a well-mixed turbulent boundary layer underneath a relatively non-turbulent free atmosphere separated by an inversion (or "transition zone"). In a zero-order model, the inversion is assumed to have zero thickness and hence profiles of conservative variables show a discontinuity or a "jump" at the inversion rather than a finite gradient (see Fig. 2.1).

In this thesis, the model was used as a diagnostic to obtain radiation, given vertical profiles of potential temperature and specific humidity. It is noted that the model also can be used to predict profiles and cloud conditions, and hence radiation at future times.

Total specific humidity, q_t, and equivalent potential temperature, Θ_e, are conserved quantities in pseudo-adiabatic processes and are thus assumed to be well-mixed within the boundary layer. They are given by the following equations:

$$q_t = q_v + q_l \ , \qquad (2.1)$$

where q_v is the water vapor mixing ratio and q_l is the liquid water mixing ratio computed using procedures by Deardorff (1976);

$$\Theta_e = \Theta + L_v/(C_p\ q_v) \ , \qquad (2.2)$$

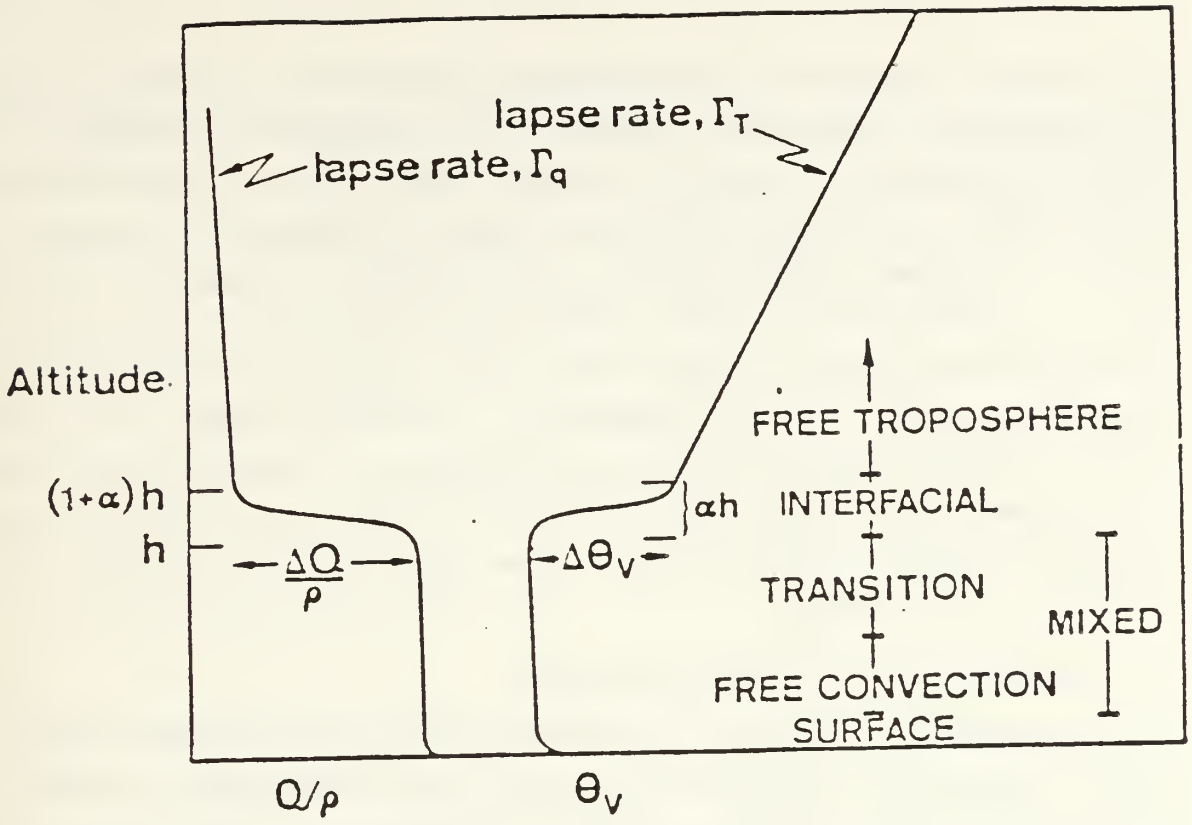

Fig. 2.1 Typical Potential Temperature and Moisture Profiles.

where Θ is the potential temperature, L_v is the latent heat of vaporization of water, C_p is the specific heat at constant pressure. A third fundamental dependent variable is the mean mixed layer depth, h.

Turbulence is responsible for the transport of kinetic energy, sensible heat and latent heat at the level of the inversion. Hence, turbulence is responsible for the coupling between the free atmosphere and the MABL. The turbulent fluxes of the temperature and humidity at the surface and the level of the inversion change the values of the well-mixed quantities over time. Large velocity fluctuations and mixing in the ABL lead to energetic eddies extending from the surface to the inversion. These eddies entrain warm, dry air into the mixed layer resulting in upward growth of the mixed layer. This is called entrainment.

Another important property of the MABL is the lifting condensation level (LCL), which is a function of temperature and humidity values in the mixed layer. The LCL determines the height at which moisture condenses within an air parcel that is lifted adiabatically. The height of the LCL relative to the height of the inversion specifies cloud formation and dissipation within the mixed layer. If the LCL is above the level of the inversion, the mixed layer is cloud free. If the LCL is below the inversion, a layer of stratus is formed, extending from the LCL to the top of the mixed layer. Stratus in the mixed layer has profound effects on the radiation budget.

A. RADIATIVE FLUX CONSIDERATIONS

Radiation, as a basic driving force of the diabatic PBL, is an important component of the surface energy budget. Cloud-radiation effects have a significant influence on vertical cloud development since radiational cloud top cooling increases convective activity (Beniston and Schmetz, 1985).

The following section describes radiation scaling in the model. It is an abbreviated version of that given by Davidson et al (1984). The cloud-shortwave radiation interactions are modeled on the assumption of solid stratocumulus cloud cover. The longwave model is based on an empirical relation of the average cloud liquid water and the cloud emissivity which may contain some slightly broken thin stratocumulus. Clearly neither radiation model applies under a field of individual optically thick clouds.

1. Longwave Radiative Flux

The longwave net radiation is the amount of upwelling longwave radiation measured at the surface which includes a positive contribution from surface emittance up and negative (downward) contributions from the cloud base and molecules including water vapor. Longwave radiation is

a function of sky temperature, water content, and cloud emissivity. The long-wave radiation flux was modified from a scheme used by Stage (1979), to permit non-black stratus clouds by introducing the emissivity, ε_c, which is a function of the total liquid water content, W,

$$\varepsilon_c = 1 - \exp(aW) , \tag{2.3}$$

and

$$W = \int_{Z_c}^{h} (\rho\, q_l)\, dZ , \tag{2.4}$$

where ρ is the density of air, q_l is the cloud liquid water specific humidity, Z is the height, Z_c is the LCL (cloud bottom) and $a = 0.158\ m^2 g^{-1}$ (Slingo et al, 1982). Since the cloud liquid water profiles are approximately linear with height, Eq. 2.4 becomes

$$W = 0.5\, \rho\, (h - Z_c)\, q_{lh} , \tag{2.5}$$

where q_{lh} is the liquid water content at the cloud top.

The long-wave cloud top net radiation flux, L_{nh} is calculated from the cloud top temperature, T_h, and the effective radiative sky temperature, T_{sky}, using the Stefan-Boltzman law

$$L_{nh} = \varepsilon_c\, \sigma\, (T_h^4 - T_{sky}^4) , \tag{2.6}$$

where σ is Stefan's constant and ε_c depends on the integrated liquid water content (see Eq. 2.3). Similarly, the flux at the cloud bottom, L_{nc}, is

$$L_{nc} = \varepsilon_c\, \sigma\, (T_s^4 - T_c^4) , \tag{2.7}$$

where T_s is the sea-surface temperature and T_c is the cloud base temperature. For the cloudy case, the model neglects the flux divergence in the clear air between the sea surface and the cloud bottom, therefore, $L_{ns} = L_{nc}$, where L_{ns} is the net longwave radiation at the surface.

Distinctions must be made for cloud-free and cloudy cases. In the cloud-free case, the net longwave flux is calculated from the water vapor and temperature profiles. The net fluxes L_{nh} and L_{nc} are calculated at Z=h and Z=0, respectively, using procedures described by Fleagle and Businger (1980). These procedures include integrating the flux emissivity profile with the previously mentioned modification, Eq. 2.3. In the cloudy case, only the $Z > h$ part of the integration is required in order to obtain the effective sky temperature.

The simplified longwave radiation equations treat the boundary layer as a two-layer model. The effects of continuum absorption are not addressed by the model. Continuum absorption by both water dimer and water vapor is important in the lower part (4 km) of the atmosphere if moisture values are large (Selby et al, 1976). This leads to a known bias in the longwave radiation calculations. This bias is to reduce downward emitted longwave radiation.

2. Shortwave Radiative Flux

The model calculates the shortwave radiation from the solar angle, which is a function of latitude, julian day and the time of day, and meteorological parameters. The meteorological parameters include liquid water mixing ratio, total mixing ratio, inversion height and mixed layer wind speed. The wind speed is used to estimate local production of aerosols. In calculating downward solar shortwave radiation received in the surface layer, the model calculates downward direct shortwave radiation and the downward diffuse shortwave radiation scattered by cloud droplets and aerosols.

The following shortwave radiative flux discussion is brief. The complete discussion and equations used in the model are given by Davidson et al (1984). A delta Eddington shortwave radiation flux calculation (Joseph et al,1976) is used in the model. The solar flux is evaluated over 15 equally spaced (0.1 μm width) bands from 0.2 μm to 1.7 μm wavelength. The incidence flux at the top of the mixed layer is obtained from the flux at the top of the atmosphere and the average transmitance in each of the fifteen bands, using the data and methods in the Smithsonian Meteorological Tables (1963). The fact that the solar flux in the model is only evaluated from absorption bands less than 1.7 μm wavelength, is a deficiency since a major water vapor absorption band is at 1.87 μm.

Absorption is due to five water vapor absorption bands centered at 0.75, 0.94, 1.10, 1.38, and 1.87 μm wavelengths. Using the water vapor absorption calculated from LOWTRAN 3B (Selby et al, 1976), the average absorption coefficients in each of the relevant 0.1 μm width bands (0.7 to 1.7) were calculated as a function of total absorber amount (precipitable water) (Davidson et al,1984).

In addition to water vapor absorption, there is scattering and absorption in the mixed layer by atmospheric particles, cloud droplets in the cloudy case and sea salt aerosols in the clear case. The short wave calculation is restricted to the region $Z_c < Z < h$. In the cloud-free case, Z_c is set to zero to include the short-wave attenuation in the entire (cloud-free) mixed layer. In the cloudy case, only the region from the cloud base up to the inversion is considered in the calculation, because aerosol scattering below the cloud base is much less than scattering above the cloud base.

The scattering properties of the particle are calculated using the Mie coefficient approximations, given by

Deirmendjian (1969), at each band wavelength for the specified particle size distribution in each layer. Particle absorption is accounted for by using the complex refractive index for pure liquid water from Hale and Querry (1973). The absorption effect of water vapor and scattering plus absorption effects of the particles are combined in the manner suggested by Lacis and Hansen (1974). The particle size spectra are specified as log-normal distributions and the scattering calculations are done for four size intervals equally spaced in log-radius space.

The sea-salt aerosol parametization is an empirical fit to data published by Fairall et al (1983). The cloud droplet spectrum is based on empirical parametizations of field measurements. The data indicate a relatively constant total number density and a steady increase in mode radius with height above the cloud base. This is because the liquid water content, which describes the droplet size distribution, depends on the height above the cloud base (LCL). Hence, shortwave cloud transmittance in the model is dependent on liquid water content (Slingo and Schrecker, 1982).

III. MILDEX DATA COLLECTION AND SYNOPTIC DISCUSSION

A. MIXED LAYER DYNAMICS EXPERIMENT (MILDEX)

The Mixed Layer Dynamics Experiment (MILDEX) is a multi-group and multi-platform experiment. The observations were taken aboard the R/V Acania as well two other platforms, the R/P Flip and R/V Wacomo. The observations were made off the central coast of California near 34° N, 124° W between 24 October 1983 and 10 November 1983 (see Fig. 3.1).

The purposes of MILDEX were:

- to provide magnitudes of air-sea exchange rates for use as boundary conditions in mixed layer modeling;
- to evaluate the drag coefficient from turbulent kinetic energy dissipation measurements and its dependence on swell amplitudes and direction;
- to provide a time series of MABL structure from radiosonde measurements for model verification;
- to provide measured radiative data for comparison with radiative transfe r algorithms developed at Scripps Institution of Oceanography;
- to evaluate the effectiveness of SODAR as a ship-borne instrument to measure changes in MABL parameters;
- to evaluate radiative transfer models of the atmosphere with cloudiness as a primary parameter.

Measurements made from the R/V Acania included those of windspeed, temperature, humidity, radiation and atmospheric pressure in the surface layer, and sea-surface temperature. Profiles of wind speed and direction, temperatures and humidity were obtained from on-board radiosonde launches. Radiosonde launches were coordinated with satellite pass times. Additionally, there were hourly observations of cloudiness and sea state. Figure 3.2 is a time series depicting the wind speed, temperature and humidity for the entire MILDEX period. A time series of net shortwave and net longwave radiation at the surface is shown in Fig. 3.3.

MILDEX 1983

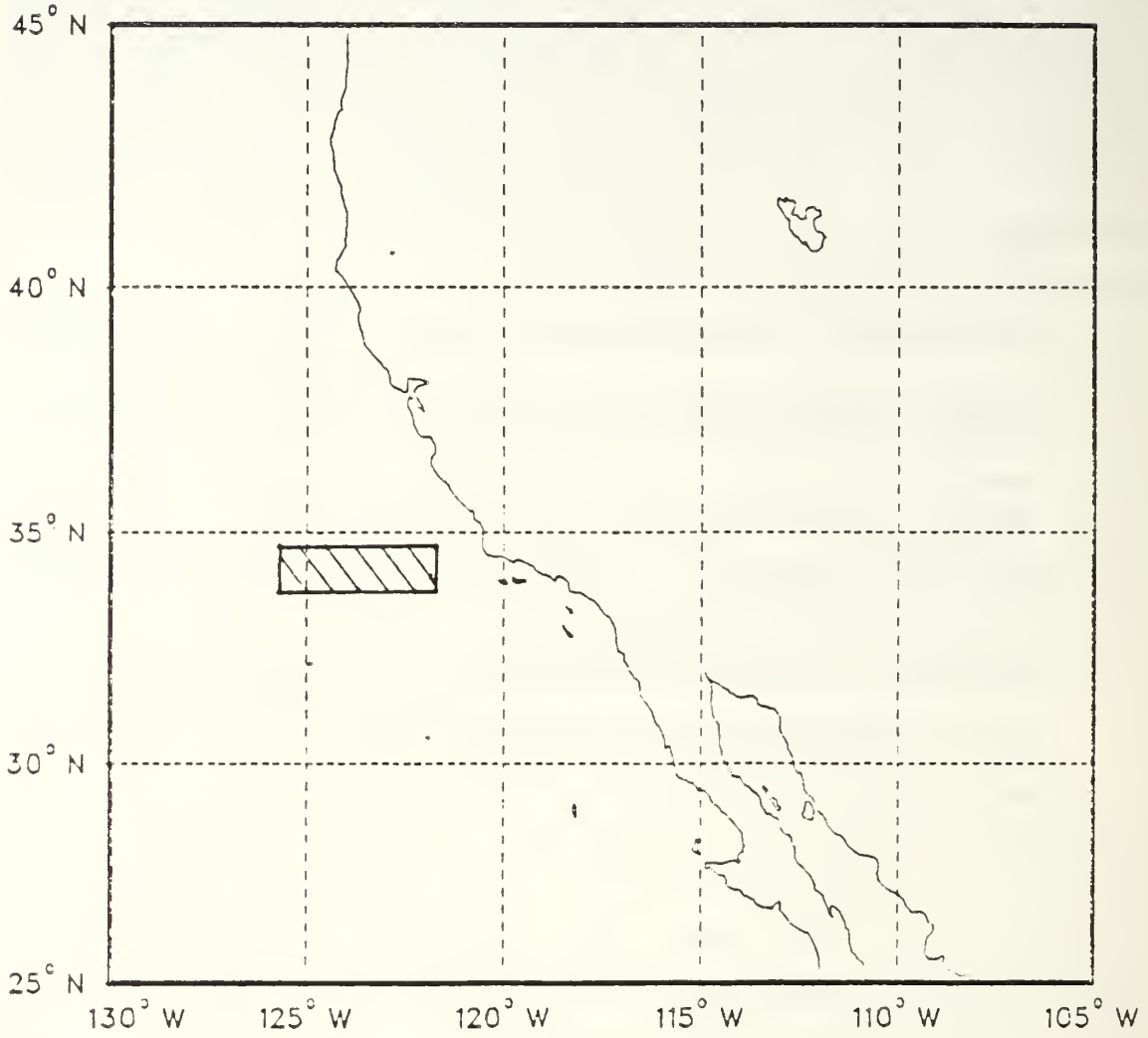

Fig. 3.1 Position of R/V Acania
Location of MILDEX (hatched) Region.

B. SYNOPTIC CONDITIONS

This section describes atmospheric conditions during MILDEX. Emphasis is placed on conditions appropriate to the mixed layer model and radiation variations. These conditions include position of fronts, cloud conditions and what clouds were observed in and above the mixed layer. Five frontal passages occurred during the MILDEX experiment. Major frontal passages occurred on 29 and 31 October, and 6 November 1983.

In the period from 25 October to 27 October, synoptic patterns were dominated by a subtropical high pressure cell. Winds were light (1-6 m/s) and northerly. Dominant clouds were stratus, stratocumulus and cirrus. The top of the inversion was near 700 m, and potential temperature and specific humidity below the inversion remained well-mixed throughout this period.

On October 28, a weak cold front began to influence conditions. By 1800GMT winds shifted to southeasterly and wind speeds decreased from 5-6 m/s to 1-3 m/s. Air temperature increased due to an advancing warm air mass. Cloud cover was mostly broken to overcast dominated by stratocumulus and altostratus (see Figs. 3.9, 3.10 and 3.12).

The front passed at 1400GMT on 29 October, even though it was not shown on the National Meteorological Center (NMC) surface analysis in Fig 3.14b. The 500 mb analysis showed hints of a 500 mb trough near 130° W, with a low at the top of the trough at 30° N. The frontal passage was determined by satellite interpretation and a time series analysis of observed winds (speed and direction), observed temperatures and pressures (see Fig. 3.2). Winds shifted from southeasterly to southerly, and wind speeds increased from 3 m/s to 12 m/s before the frontal passage and then decreased to 2 m/s after frontal passage. The warm sector preceding a second cold front increased the temperature by two degrees.

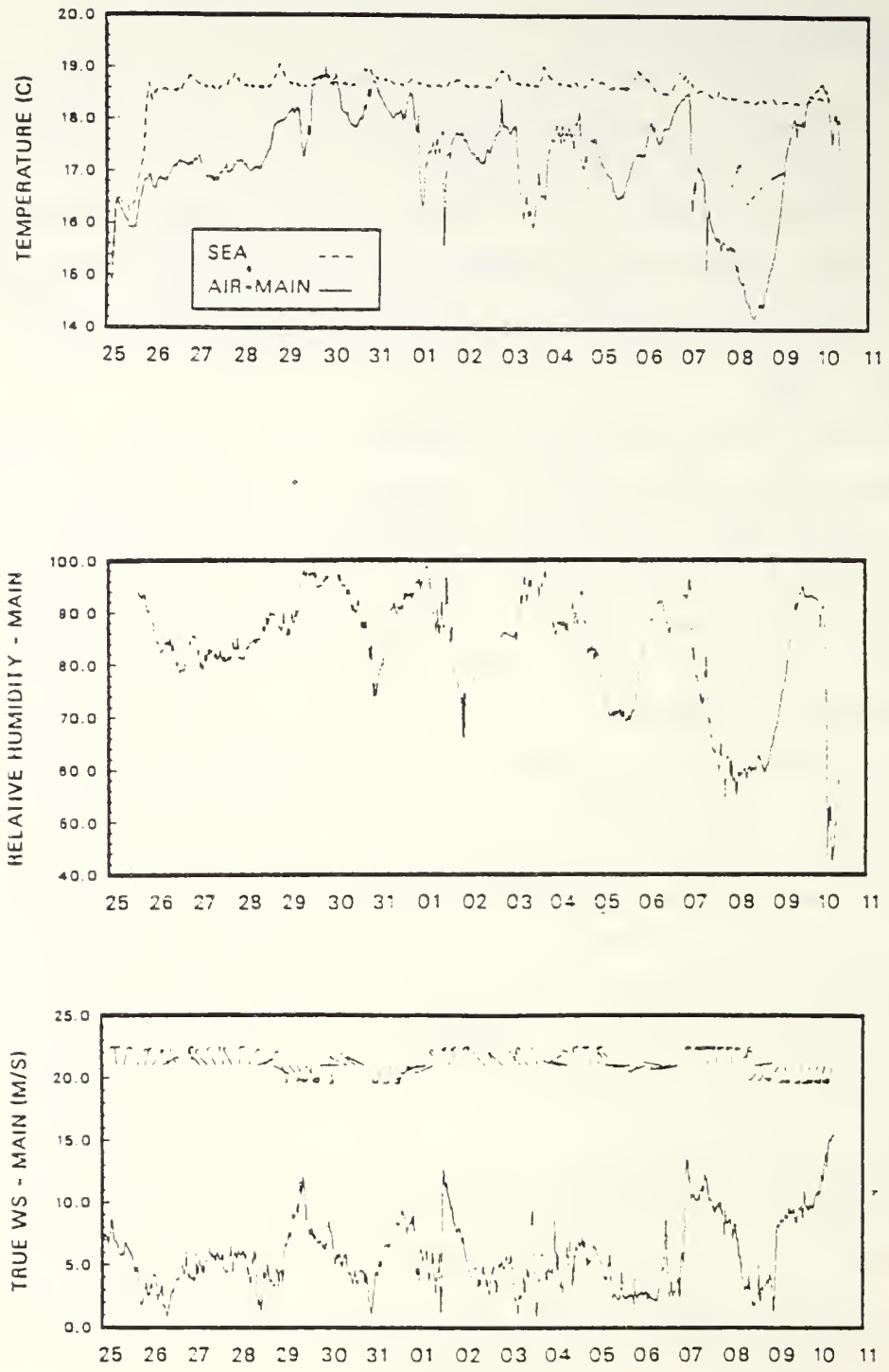

Fig. 3.2 A Time Series of Temperature, Relative Humidity and Wind Speed valid from 26 October to 9 November 1983.

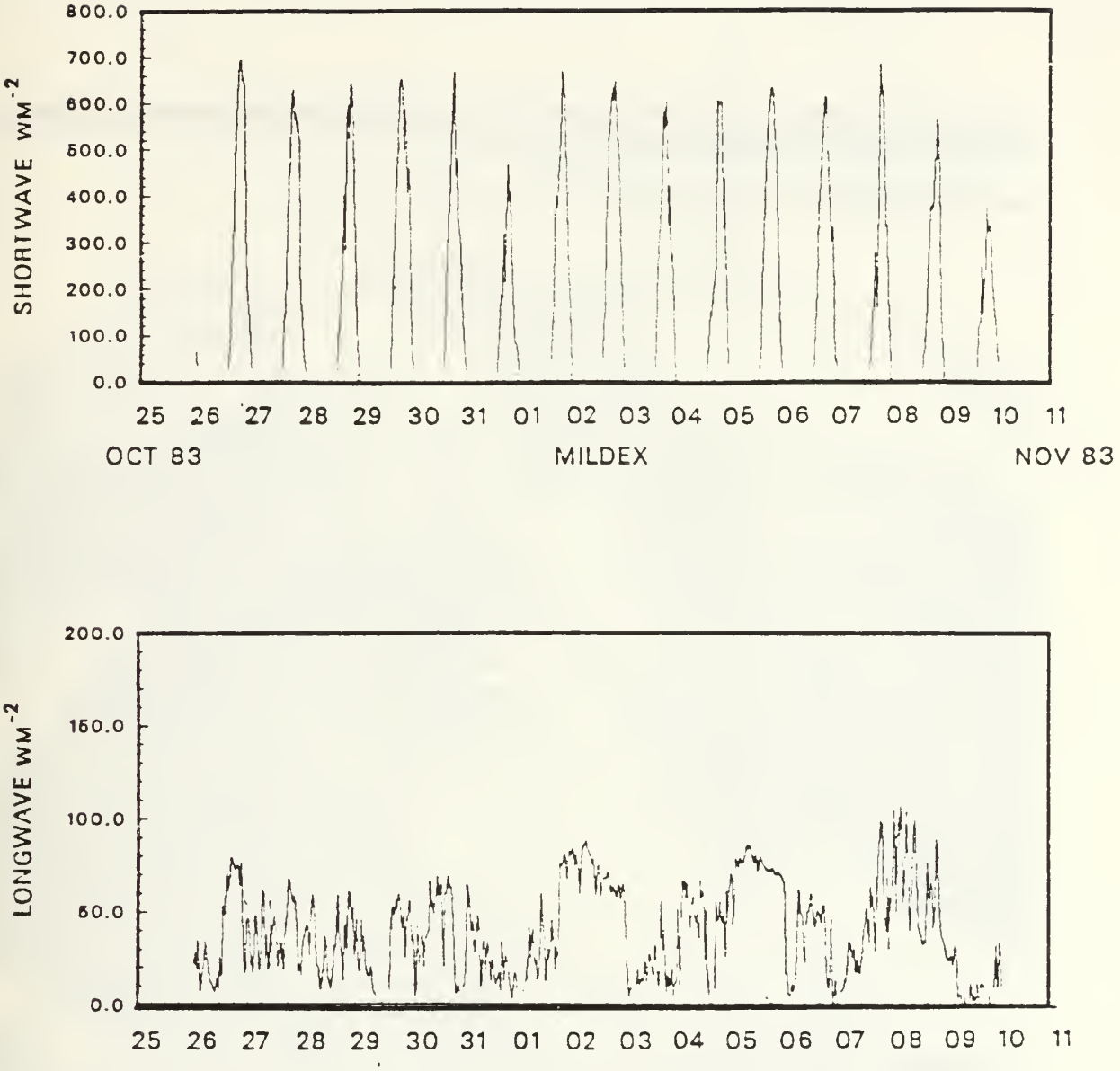

Fig. 3.3 A Time Series of Shortwave, and Longwave Radiation valid from 26 October to 9 November 1983.

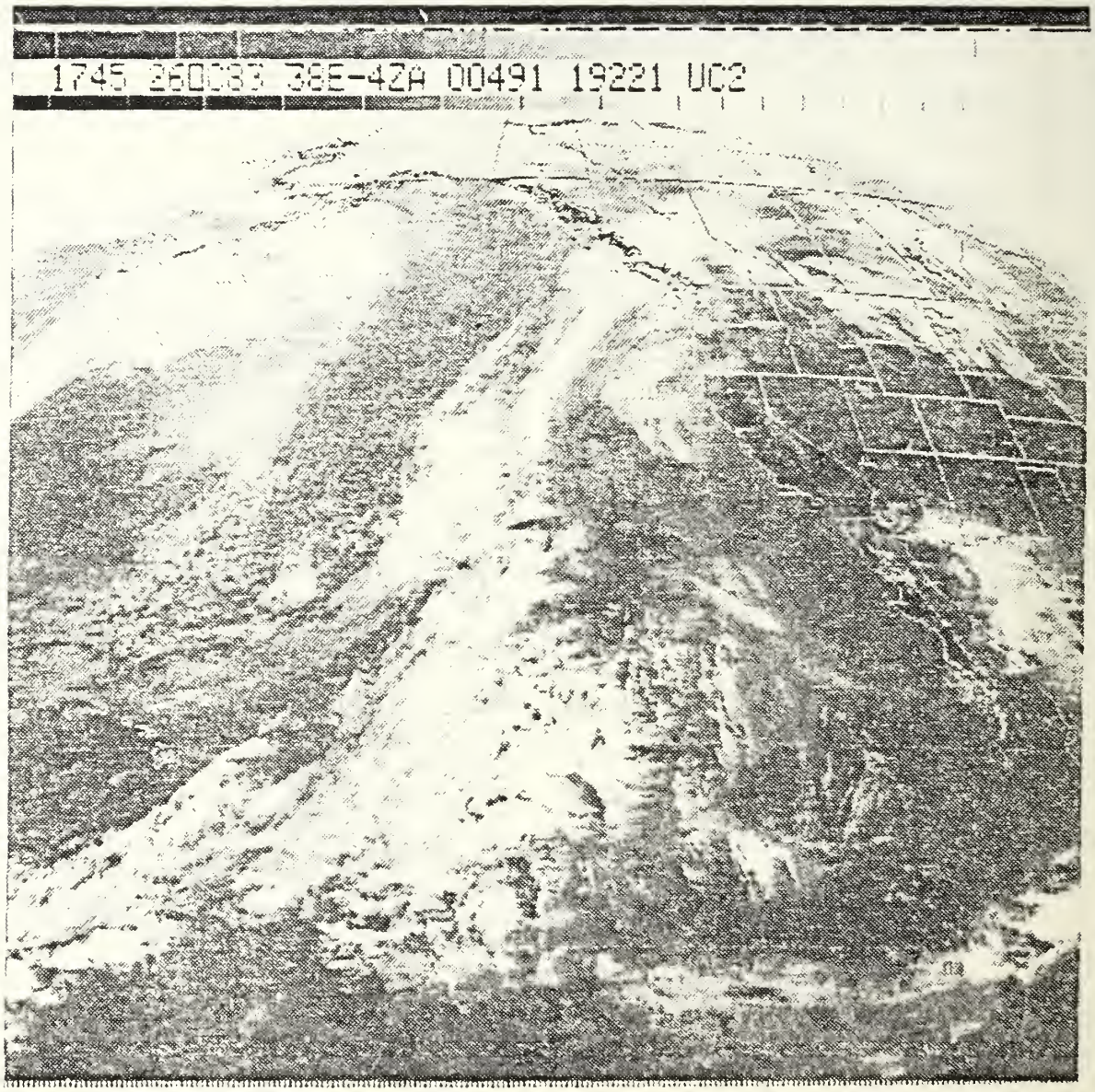

Fig. 3.4 26/1745GMT October 1983 Satellite Picture.

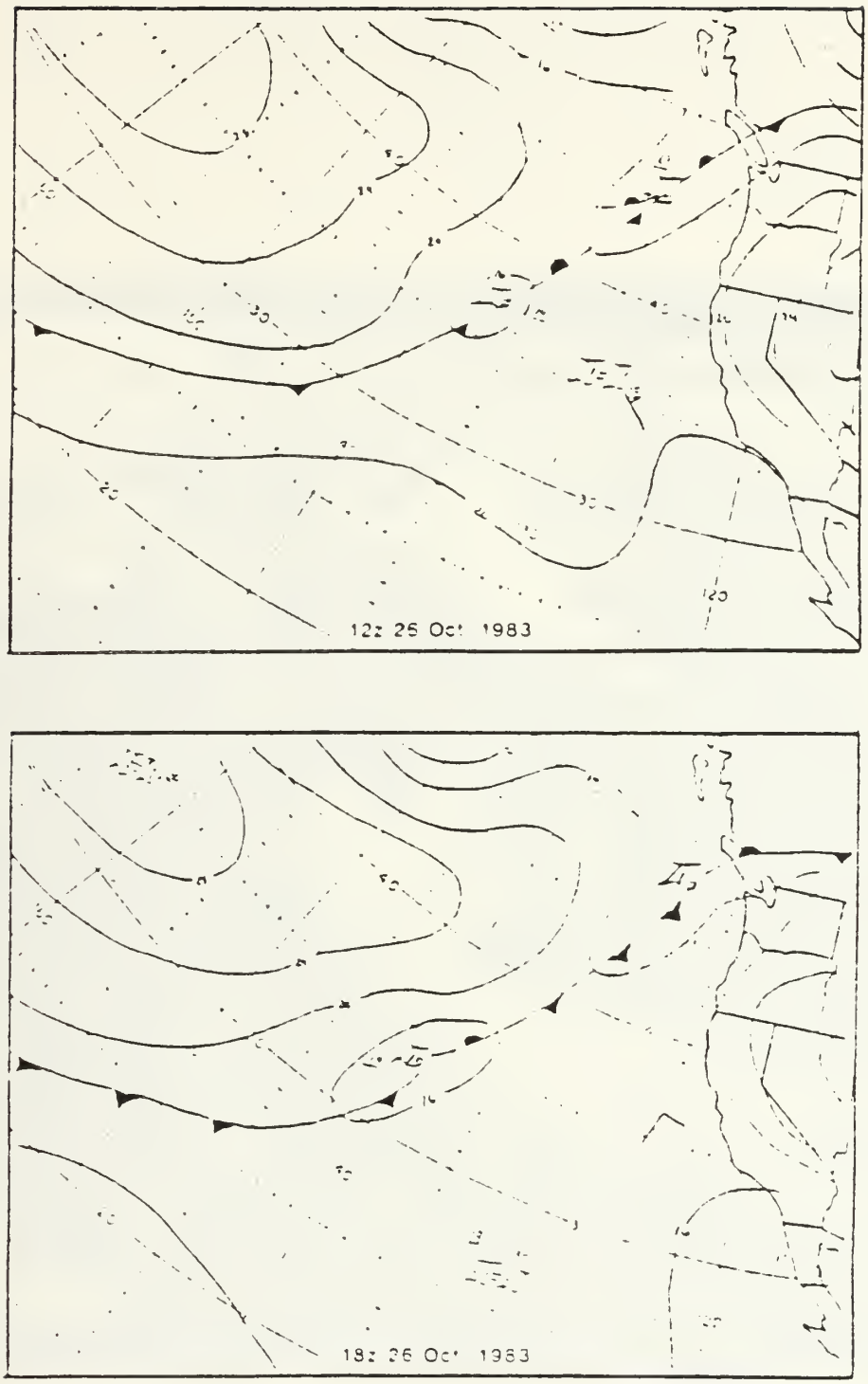

Fig. 3.5 26 October 1983 Surface Charts
a) 1200GMT (top), b) 1800GMT (bottom).

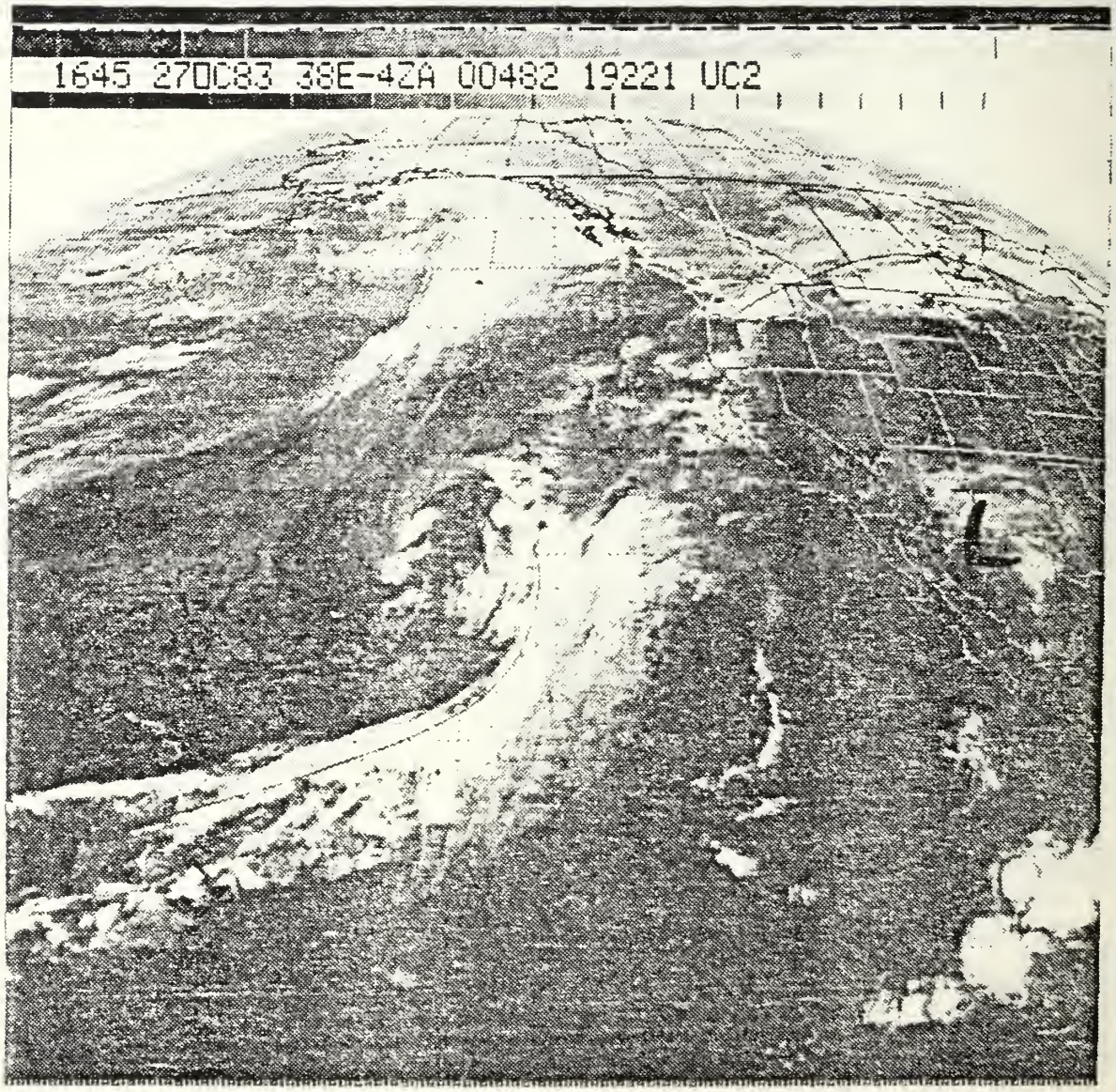

Fig. 3.6 27/1645GMT October 1983 Satellite Picture.

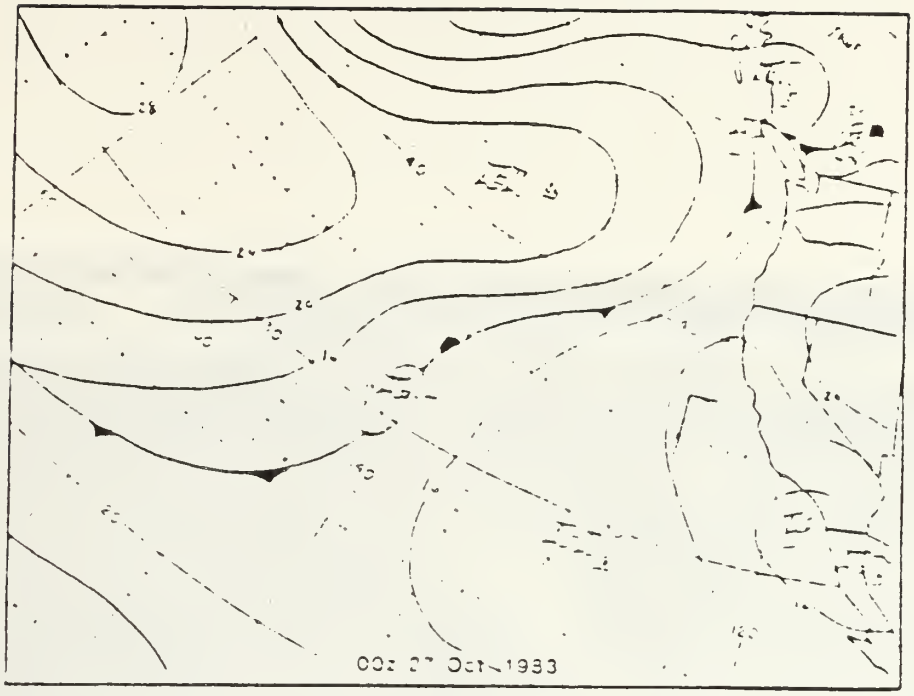

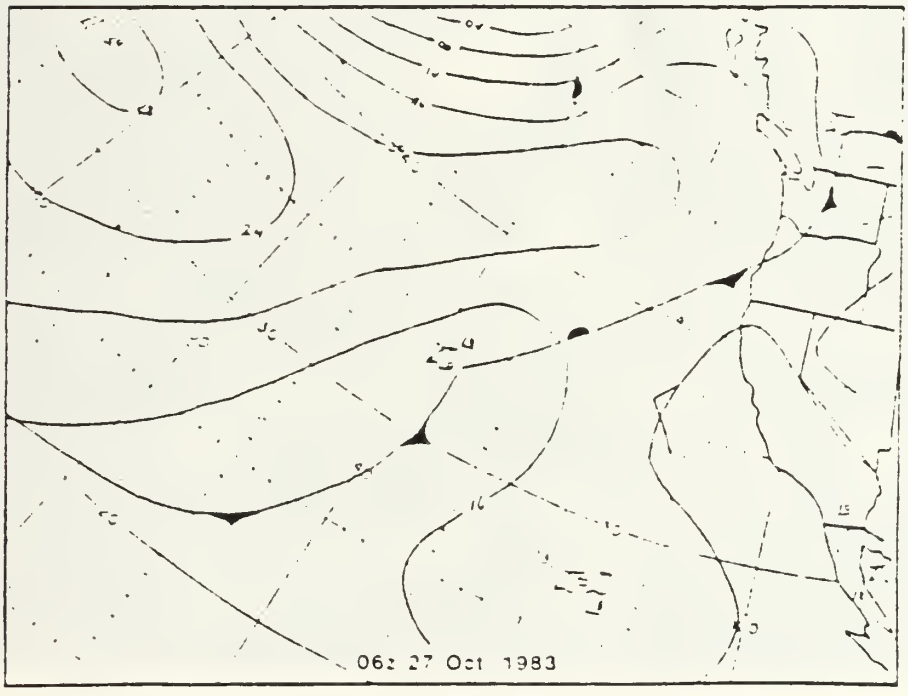

Fig. 3.7 27 October 1983 Surface Charts
a) 0000GMT (top), b) 0600GMT (bottom).

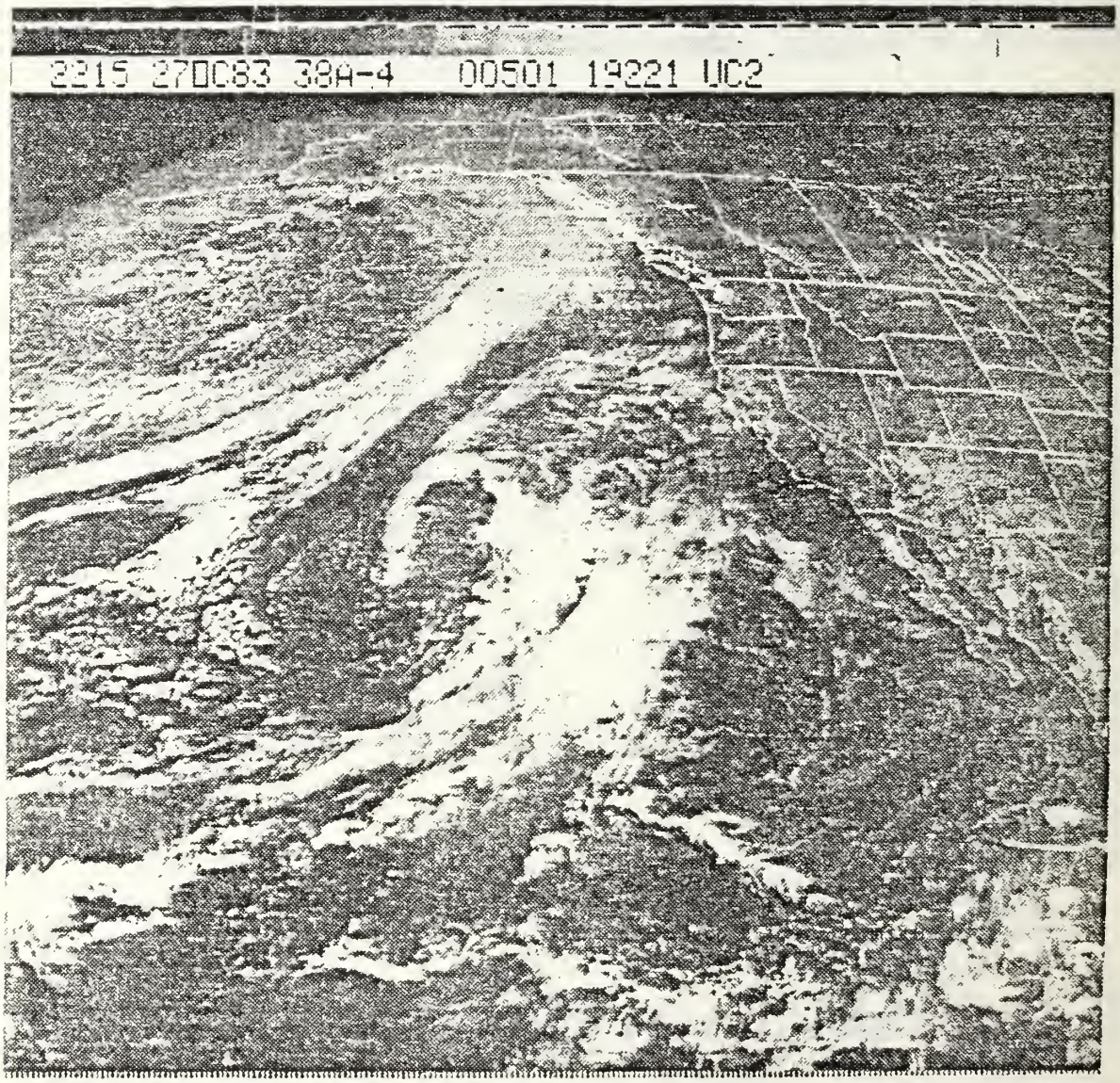

Fig. 3.8 27/2215GMT October 1983 Satellite Picture.

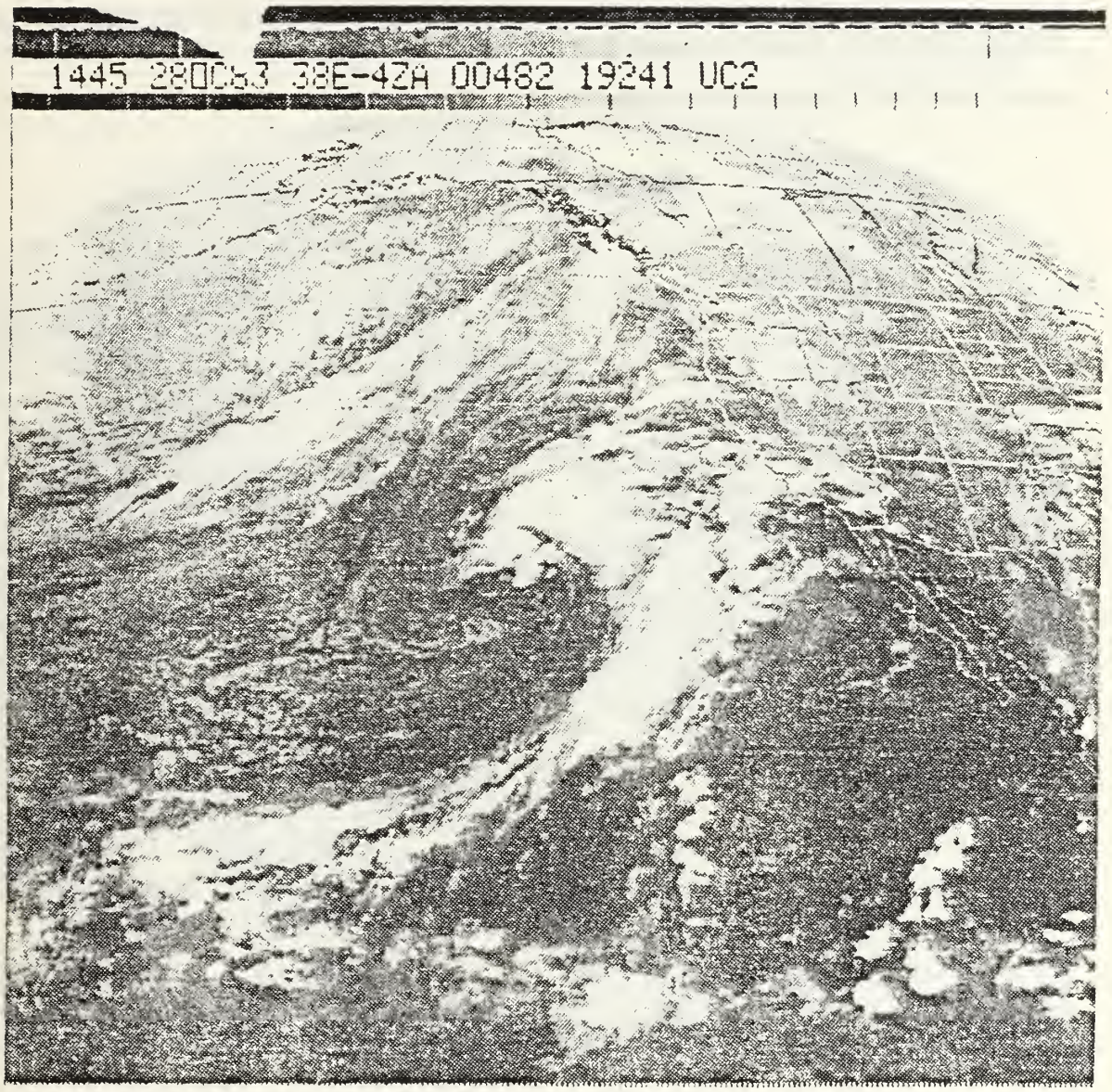

Fig. 3.9 28/1445GMT October 1983 Satellite Picture.

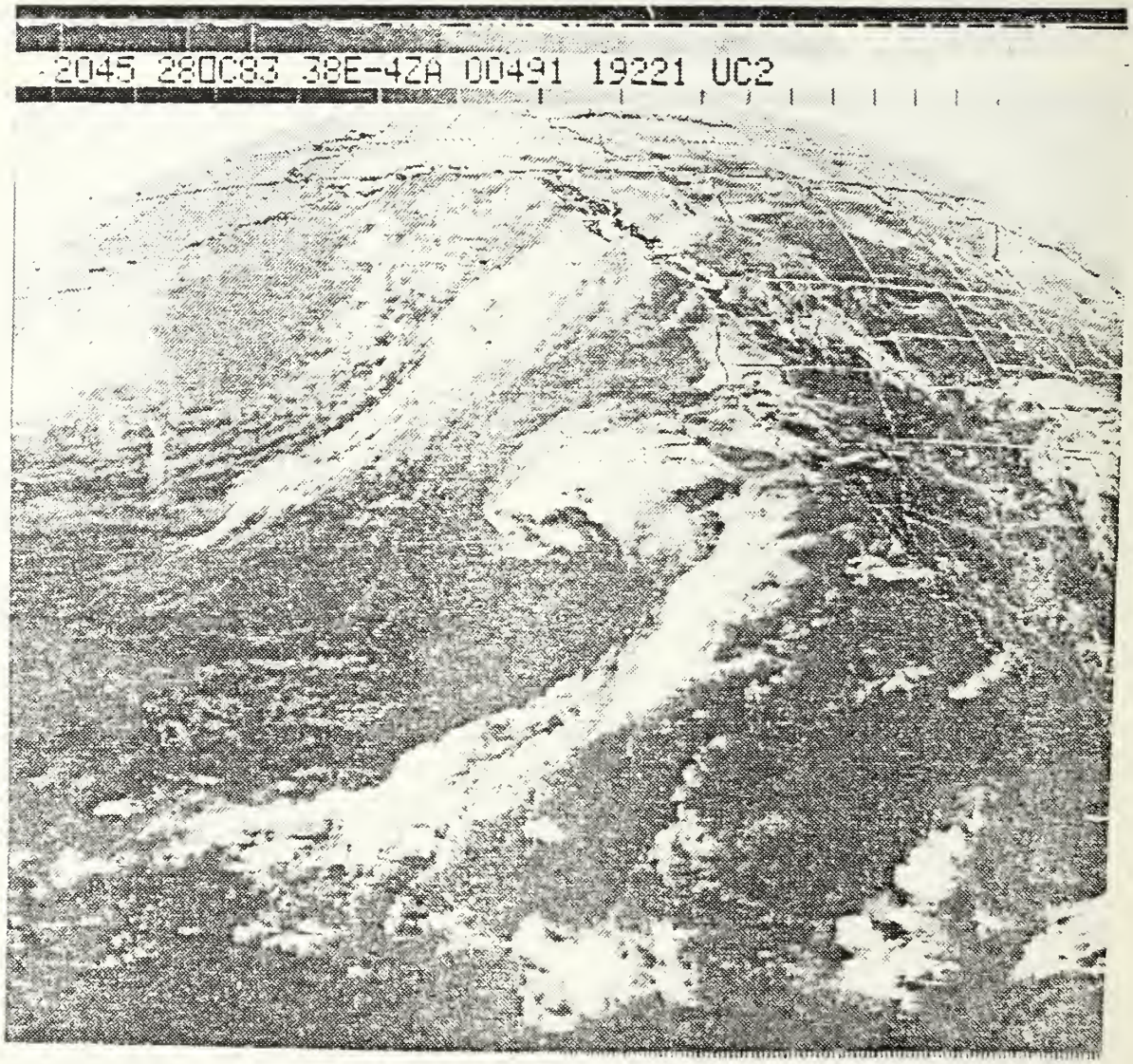

Fig. 3.10 28/2045GMT October 1983 Satellite Picture.

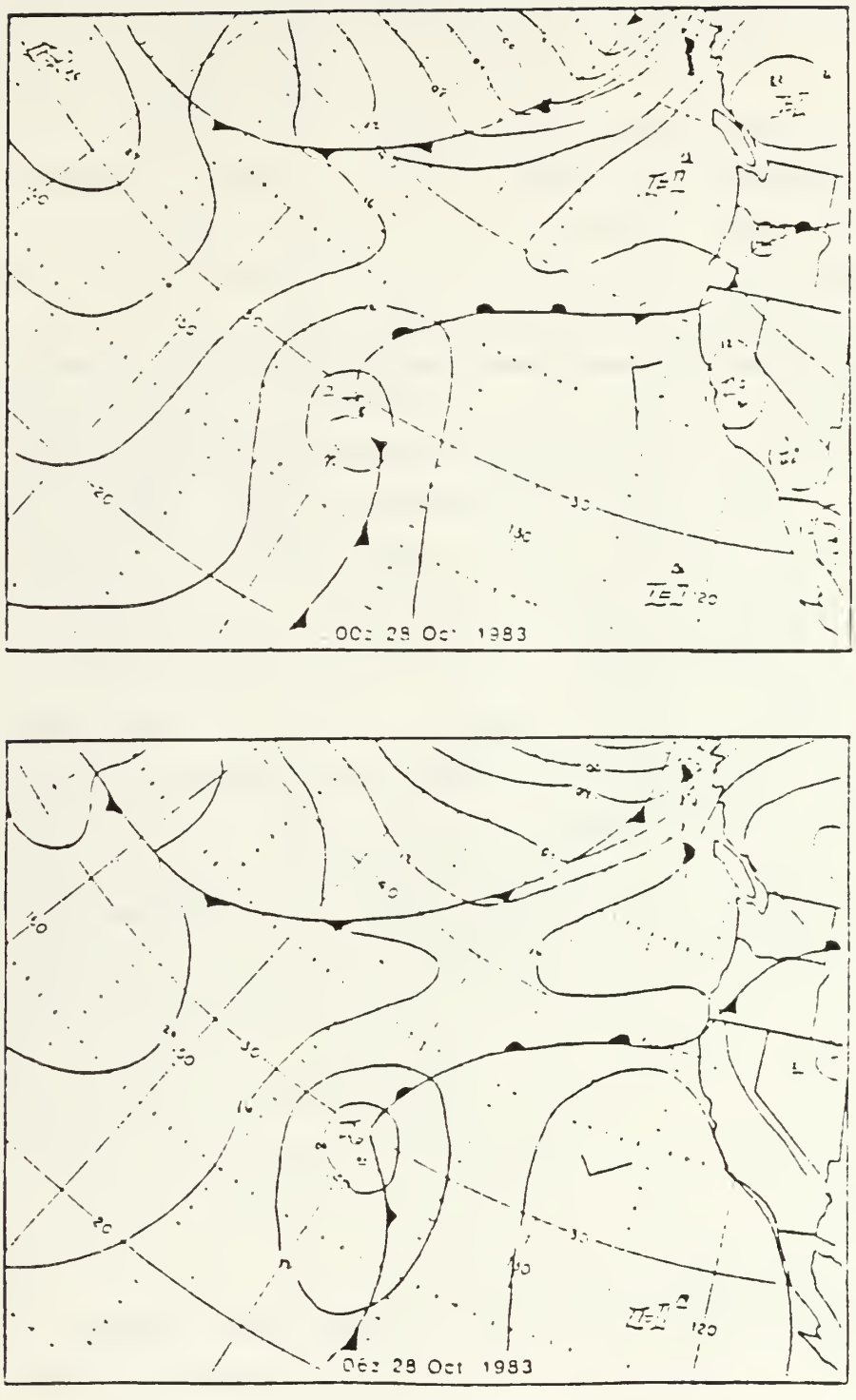

Fig. 3.11 28 October 1983 Surface Charts
a) 0000GMT (top), b) 0600GMT (bottom).

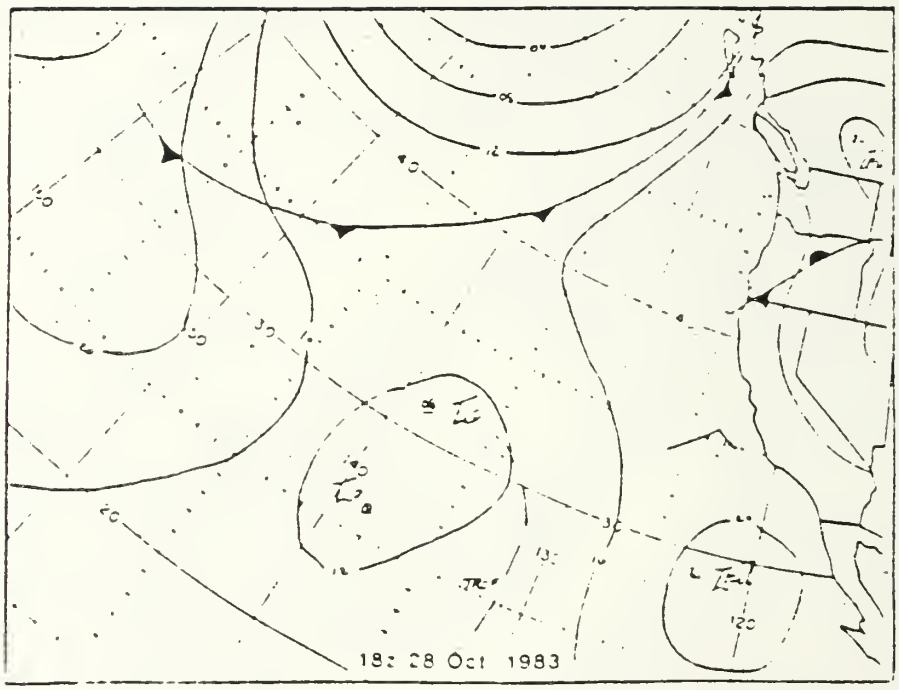

Fig. 3.12 28 October 1983 1800GMT Surface Chart.

Cloud cover ranged from scattered to overcast. Cumulonimbus clouds were reported at 1500GMT, along with rain from 0600GMT to 1400GMT (see Fig. 3.13).

On 30 October 1983, the next cold front remained west of the experiment region. Surface pressures increased, and the wind shifted from southerly to westerly with wind speed steadily decreasing from 8 m/s to 2 m/s. Air temperatures fell one degree. The cloud cover was clear to scattered with cumulus and stratocumulus clouds present (see Fig. 3.15a).

A weak cold front passage was reported by the R/V Acania at about 1700GMT on 31 October (see Figs. 3.15b, and 3.16). The synoptic picture shows a low in the eastern north Pacific Ocean, and a high dominating the Pacific north of Hawaii. The entire period was characterized by a 100% ceiling and intermittent rain and drizzle. Several squall lines were noted after the frontal passage. The clouds were mainly altostratus before the frontal passage and stratus after the frontal passage. The winds shifted from south southwest to west after frontal passage. The wind speed was 7 to 9 m/s ahead of the front and 3 to 5 m/s behind it. The air temperature dropped by 1.5 degrees centigrade after the front went by.

The passage of the third cold front occurred on 1 November 1983 at approximately 1200GMT, accompanied by a deep 500 mb trough with a northwest to southeast tilt (see Figs. 3.17 and 3.18). The winds shifted from westerly to northwesterly with wind speeds increasing to 12 m/s at 1600GMT. During a 30-minute period, the temperature dropped by 1.5 degrees centigrade. Over the next two days, the subtropical high pressure cell re-established itself. Wind directions were northerly to northwesterly, at speeds of 2 to 5 m/s. The temperature began to drop on November 3, with patches of fog, rain, and drizzle reported throughout the

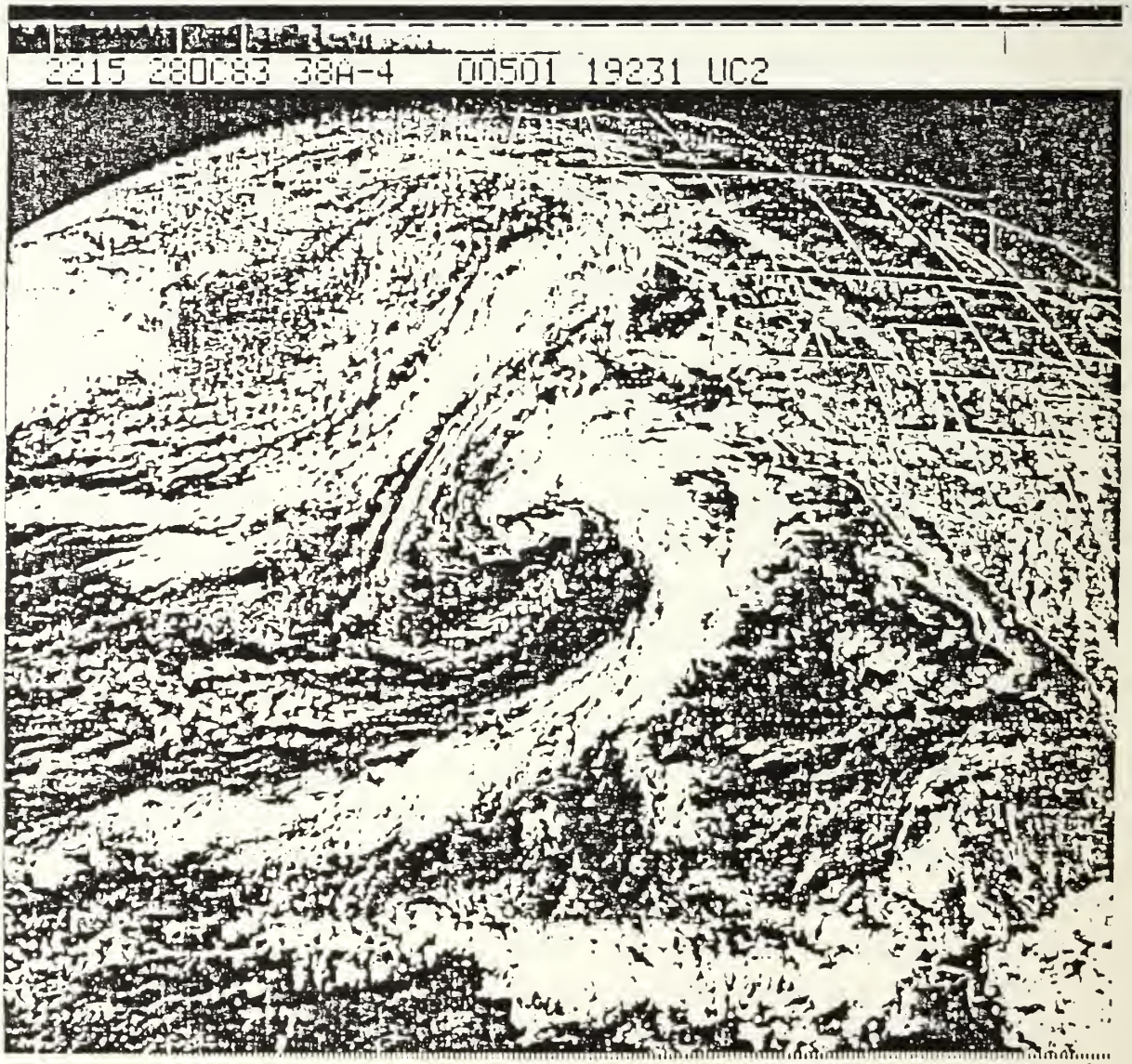

Fig. 3.13 28/2215GMT October 1983 Satellite Picture.

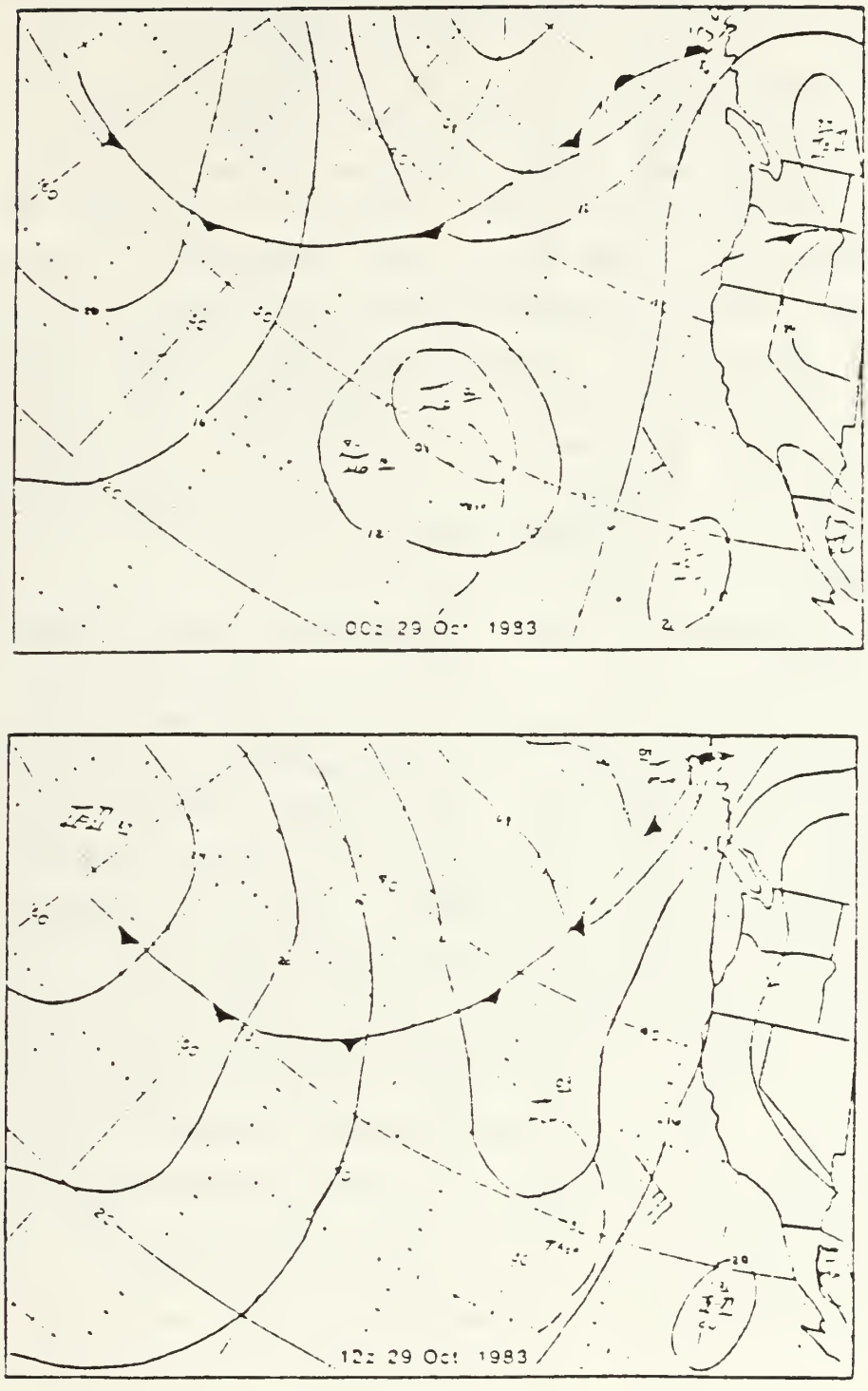

Fig. 3.14 29 October 1983 Surface Charts
a) 0000GMT (top), b) 1200GMT (bottom).

day, as a stronger cold front was approaching (see Fig. 3.19).

The synoptic pattern for 4 November 1983 showed a low center in the Gulf of Alaska, and a high building west of Baja California and south of the experimental region . No frontal passage was observed. Winds were generally from the north shifting to the west, then returning to the north, while wind speed fluctuated from 3 to 7 m/s. The surface pressure and the air temperature were nearly steady. As seen on the satellite pictures (see Figs. 3.20, and 3.21), it was overcast in the late afternoon on 3 November, with total clearing at night, and overcast again by mid-morning of the 4th. Fog, cumulus, and stratus were observed in the afternoon of the 4th (see Fig. 3.23).

The experimental region came under the influence of a weak pressure cell on 5 November, located to the south. Another low came in northwest of the experimental site, with an associated cold front. By 6 November, the warm sector of the fourth cold front began to influence synoptic conditions (see Figs. 3.26, and 3.28a). Winds, which were southwesterly, increased in speed from 2 to 13 m/s. The advancing warm air mass increased air temperature by 1.2 degrees centigrade. Cloud cover was broken most of the day, with cumulus and stratus increasing during the evening due to the approaching front. Sea level pressure increased to a maximum after the cold front passed at 0000GMT on the 7th of November (see Fig. 3.28b). The wind shifted to northerly with wind speeds averaging 10 m/s. A 500 mb ridge followed the front and was over the experimental site at approximately 1200GMT on the 8th (see Figs. 3.29, and 3.31a).

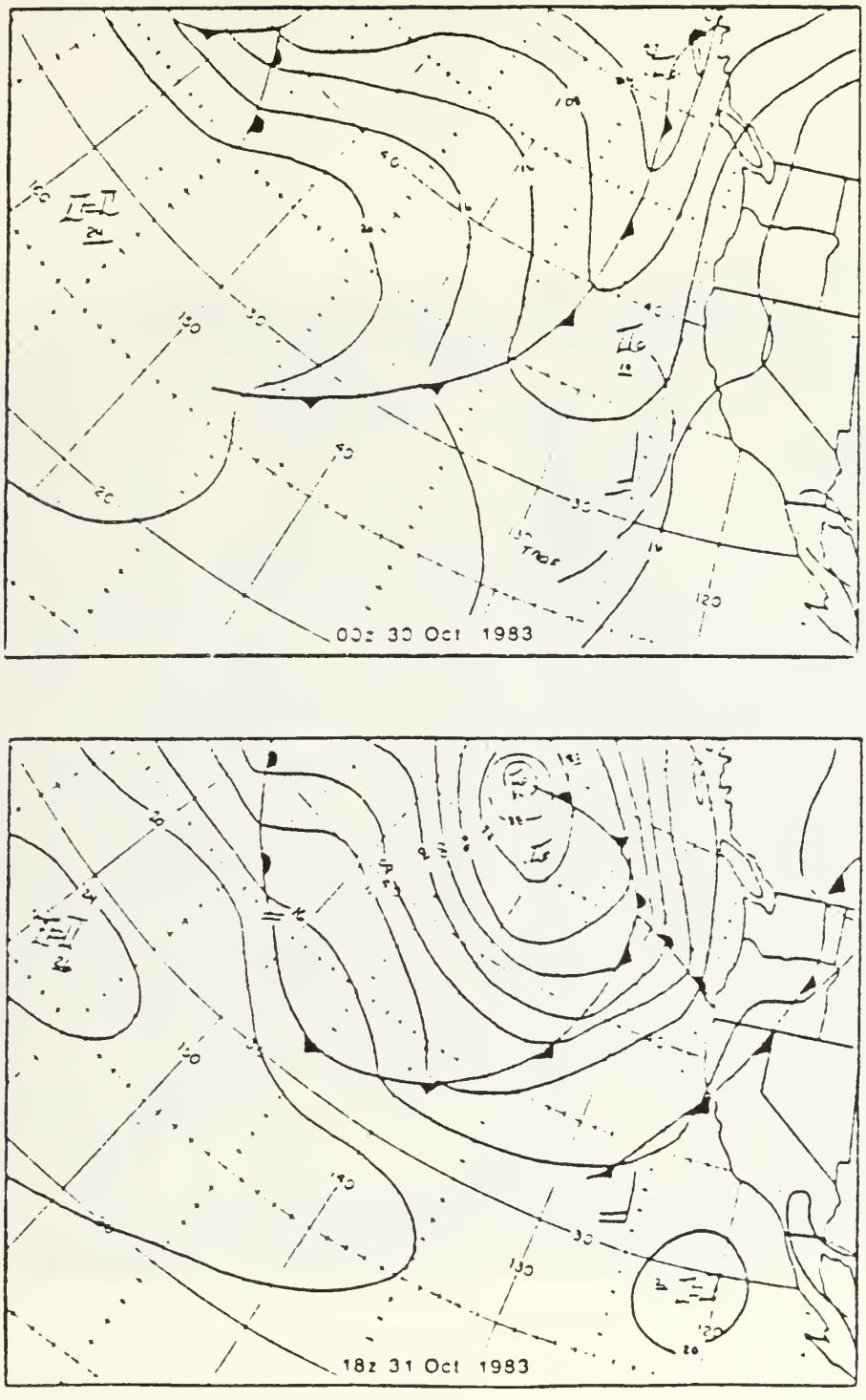

Fig. 3.15 30 - 31 October 1983 Surface Charts
a) 30/0000GMT (top), b) 31/1800GMT (bottom).

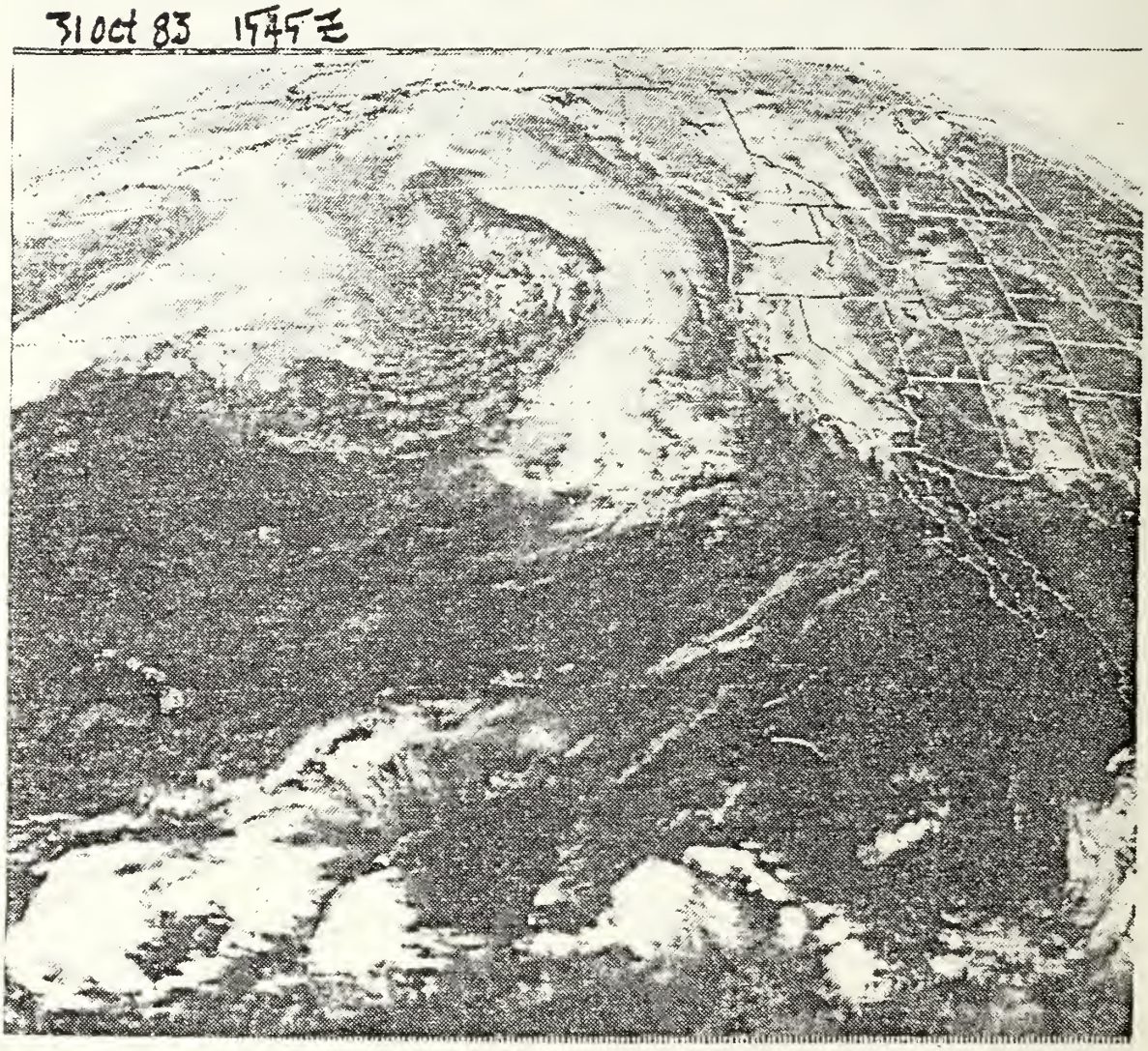

Fig. 3.16 31/1545GMT October Satellite Picture.

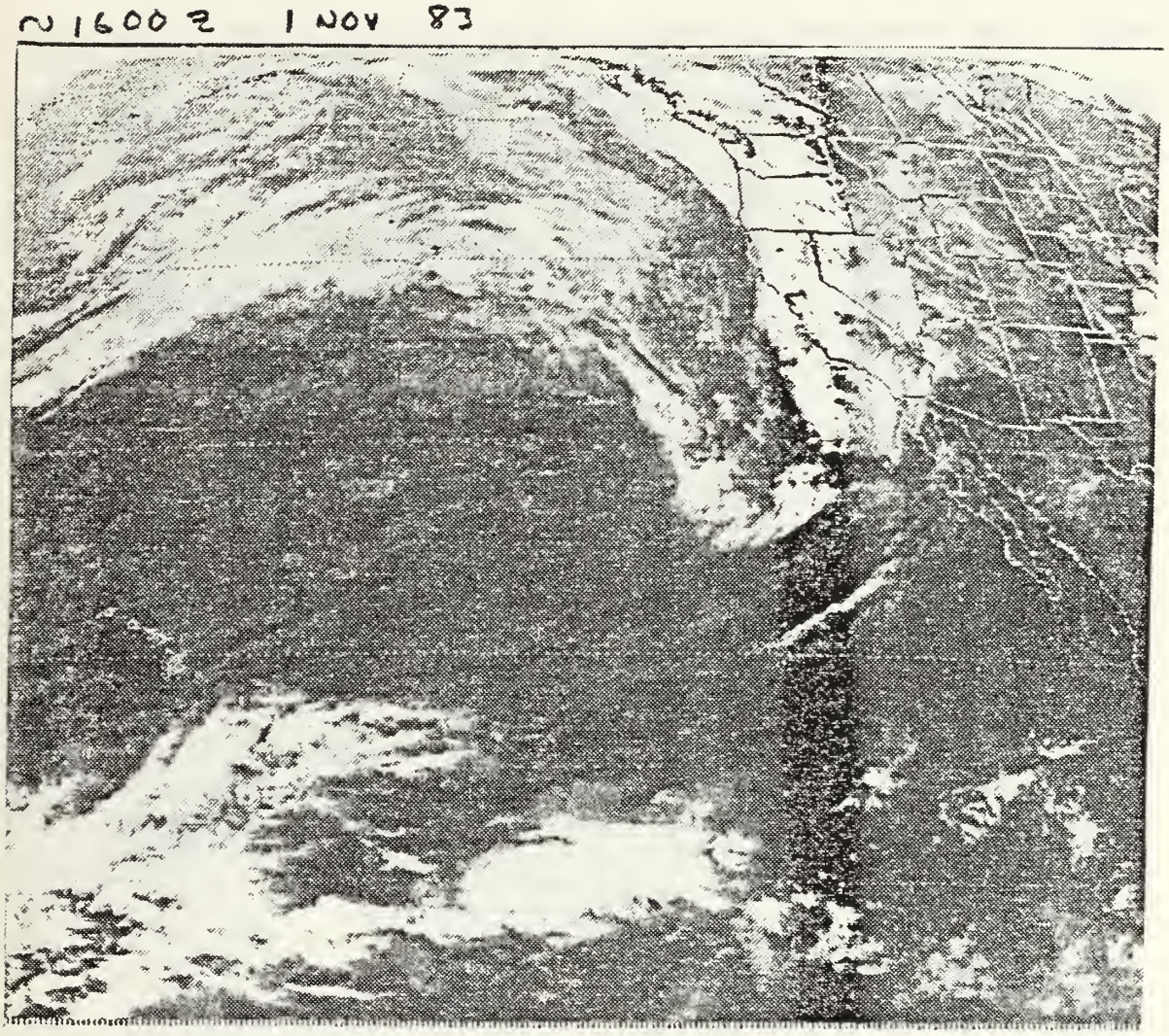

Fig. 3.17 1/1600GMT November 1983 Satellite Picture.

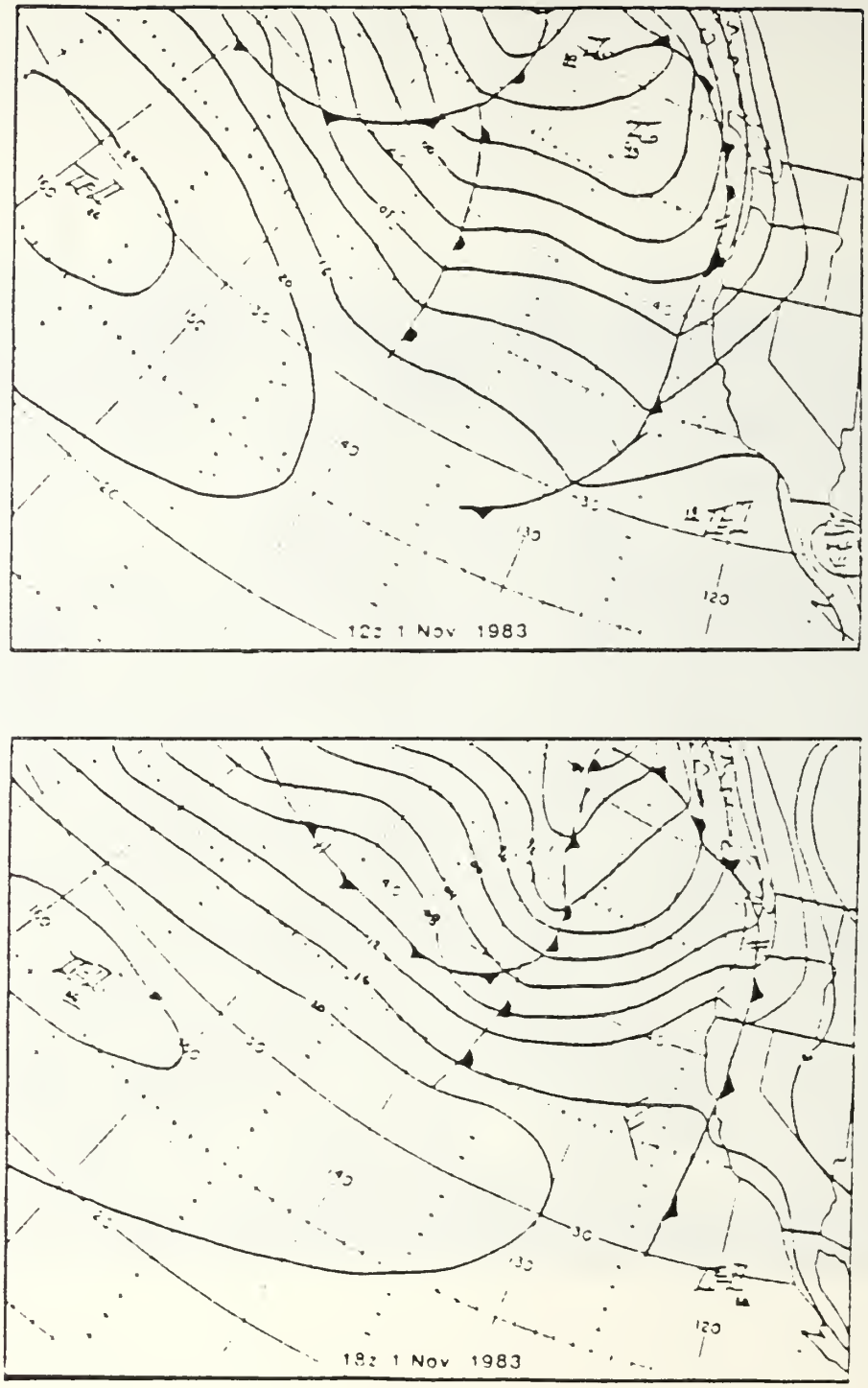

Fig. 3.18 1 November 1983 Surface Charts
a) 1200GMT (top), b) 1800GMT (bottom).

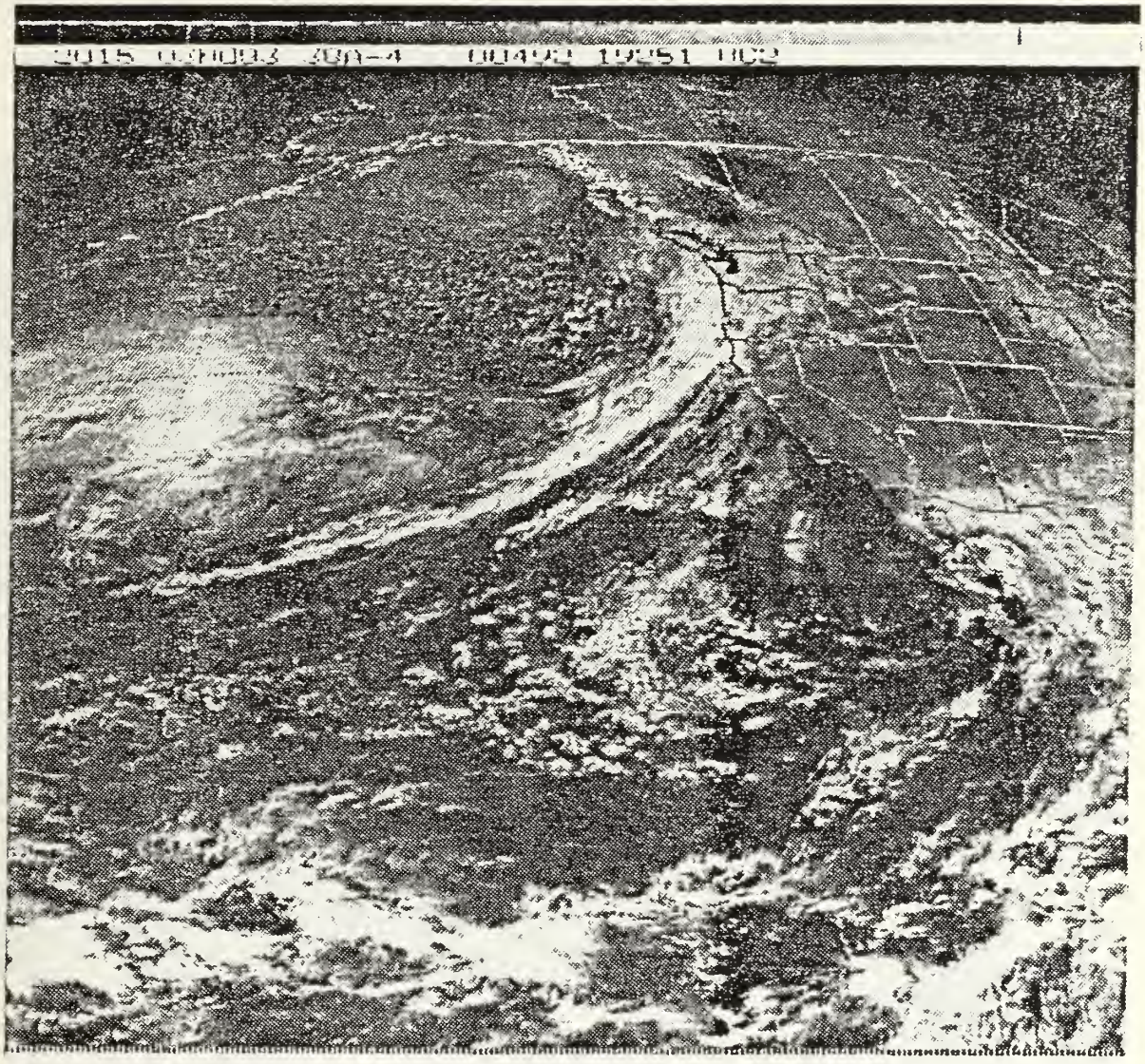

Fig. 3.19 3/2015GMT November 1983 Satellite Picture.

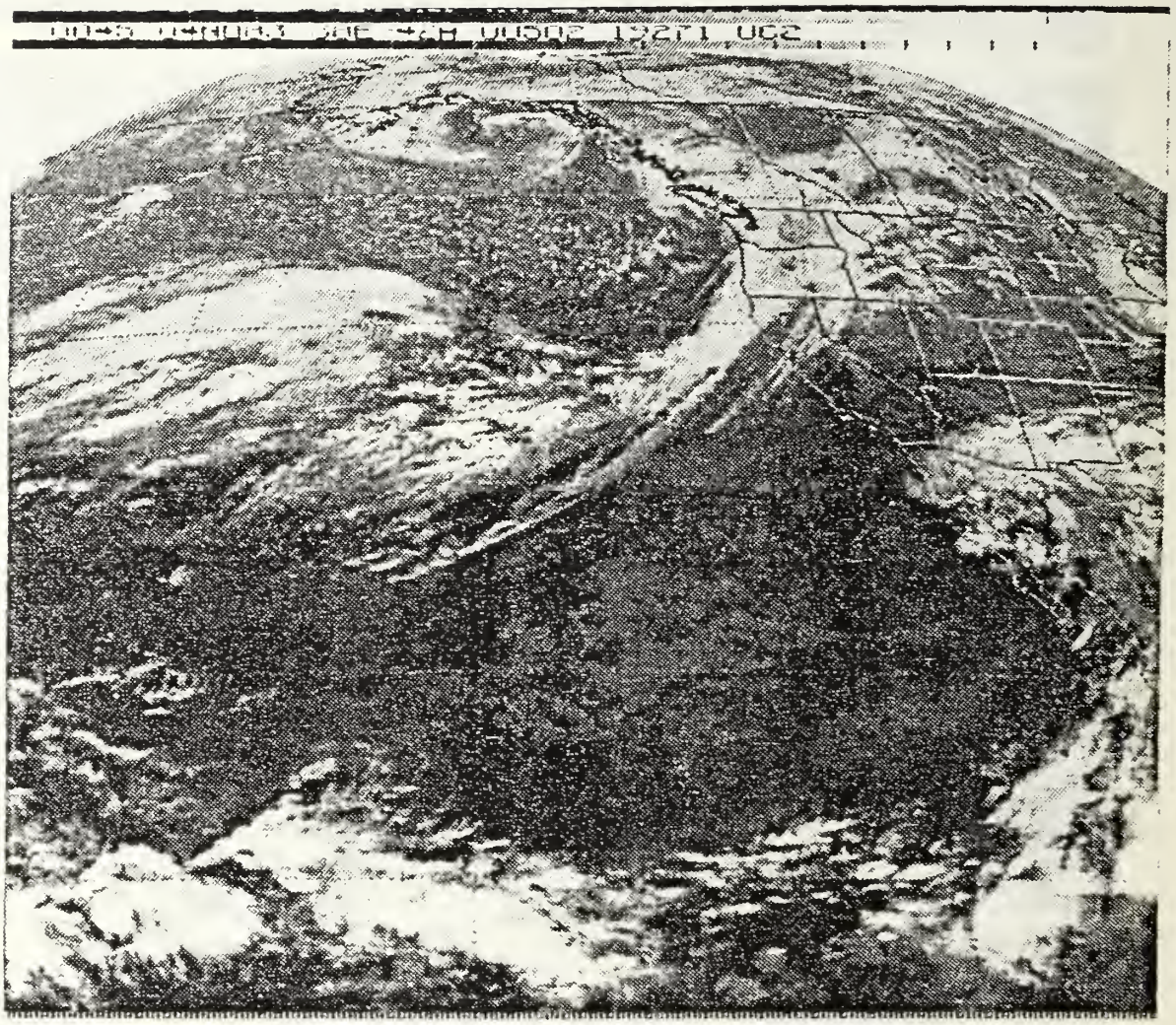

Fig. 3.20 4/0045GMT November 1983 Satellite Picture.

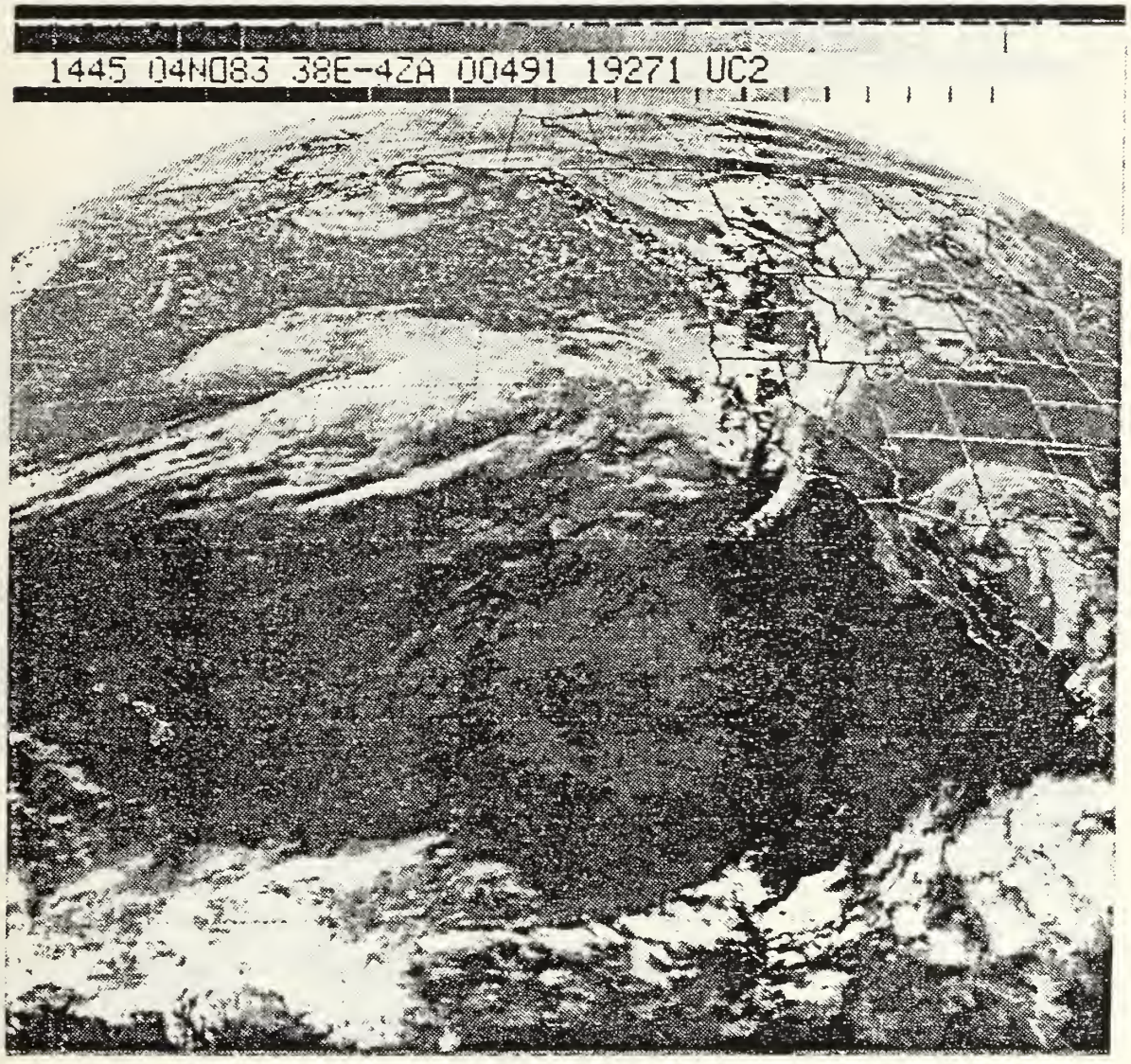

Fig. 3.21 4/1445GMT November 1983 Satellite Picture.

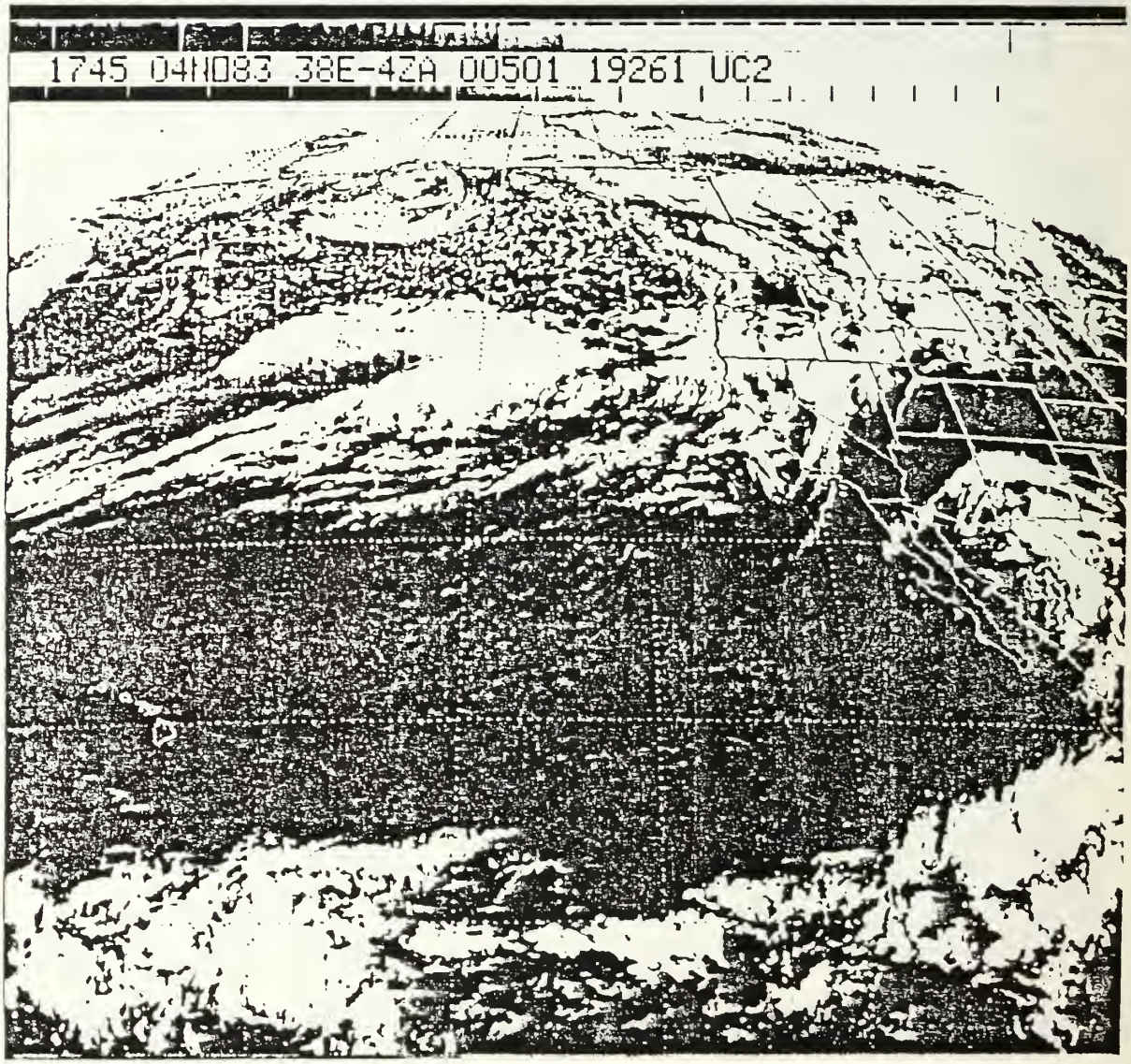

Fig. 3.22 4/1745GMT November 1983 Satellite Picture.

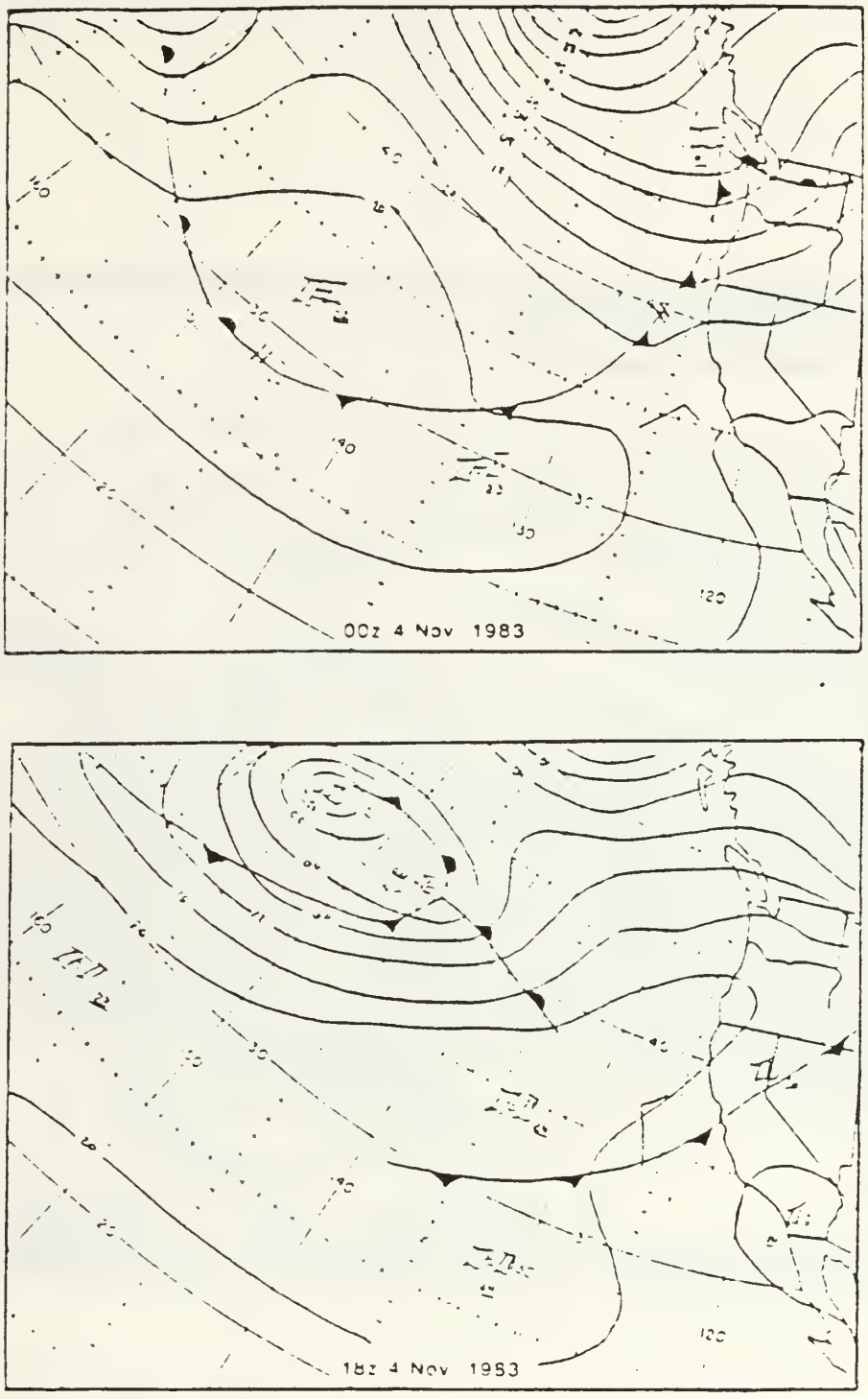

Fig. 3.23 4 November 1983 Surface Charts
a) 0000GMT (top), b) 1800GMT (bottom).

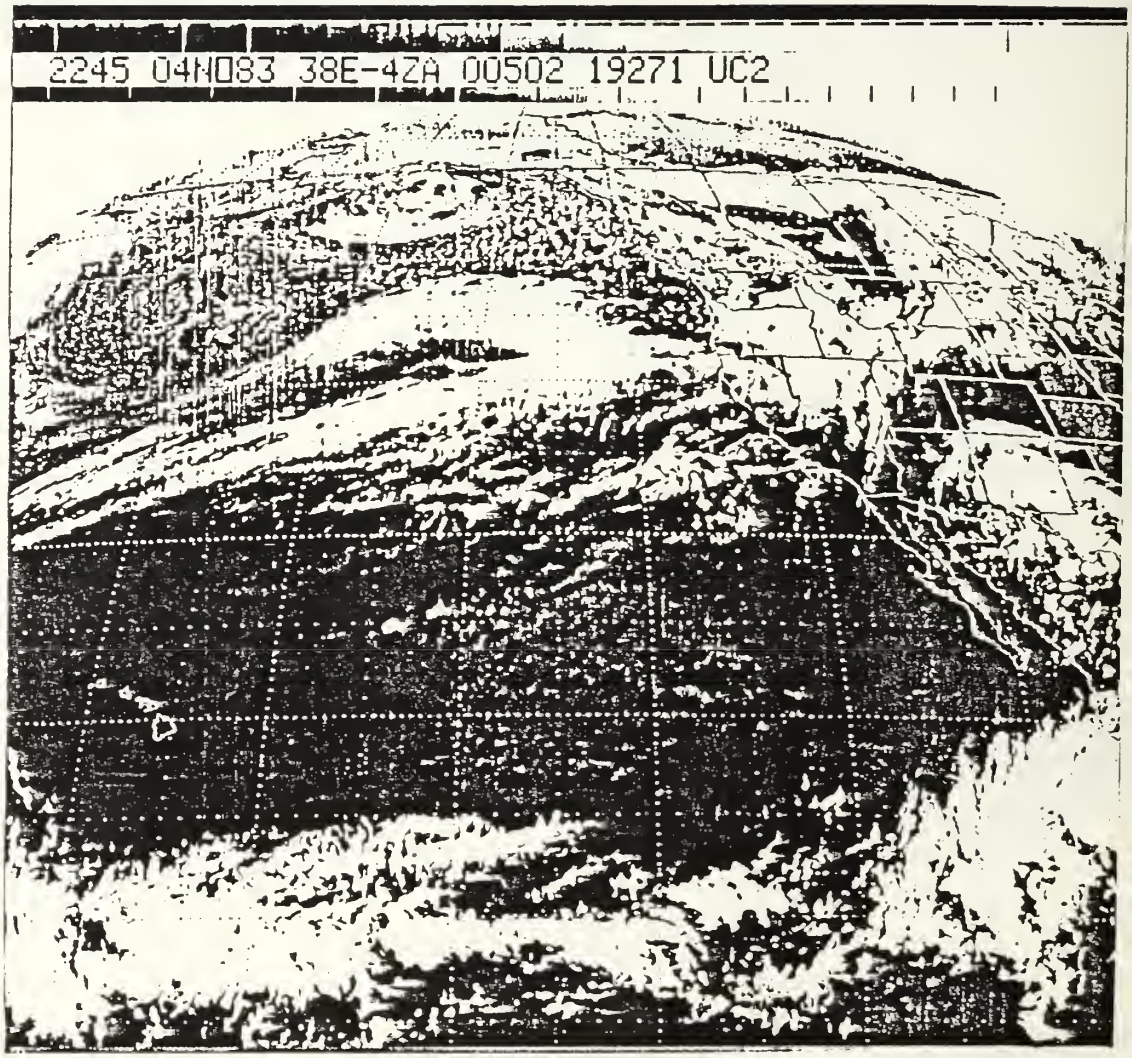

Fig. 3.24 4/2245GMT November 1983 Satellite Picture.

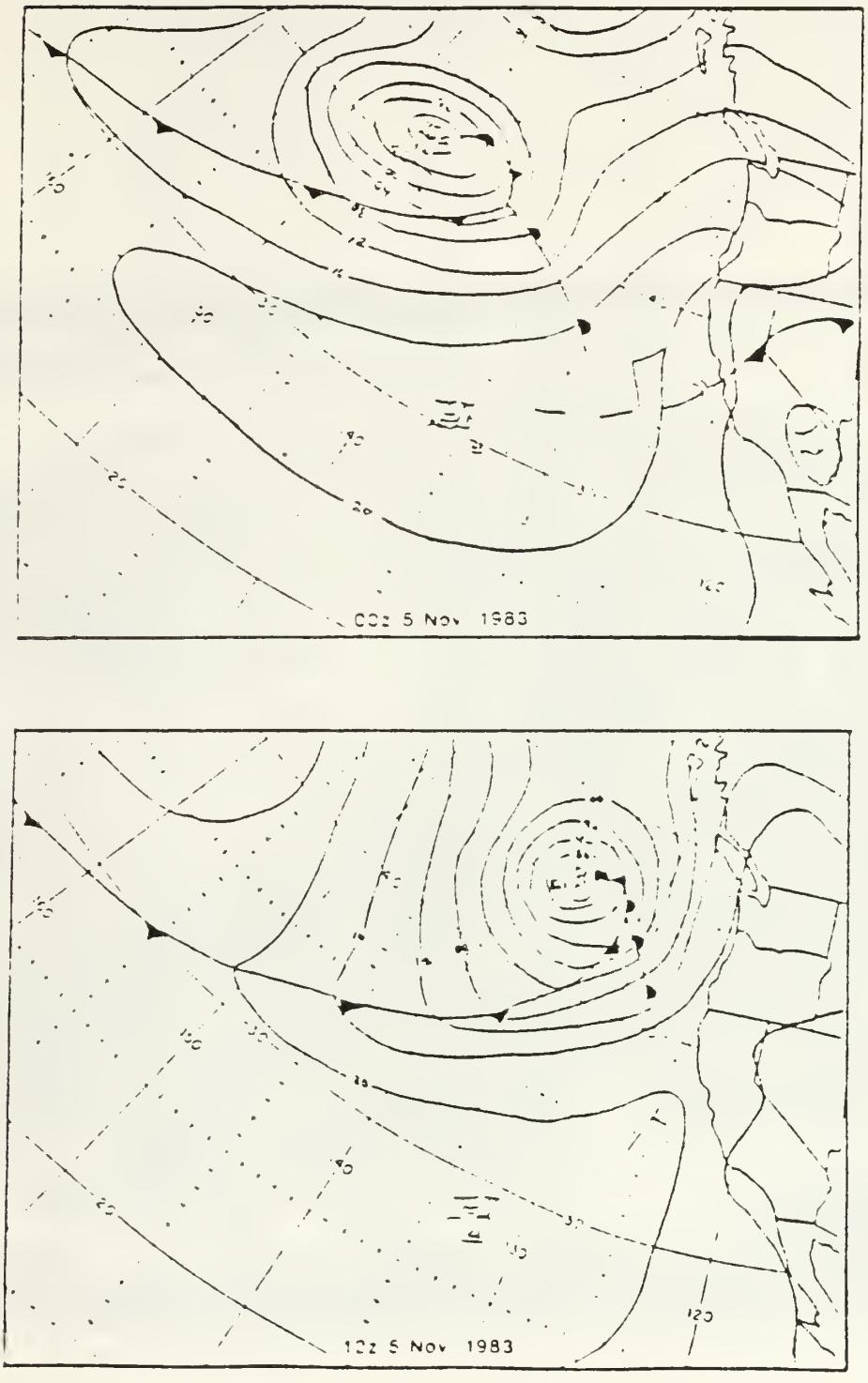

Fig. 3.25 5 November 1983 Surface Charts
a) 0000GMT (top), b) 1200GMT (bottom).

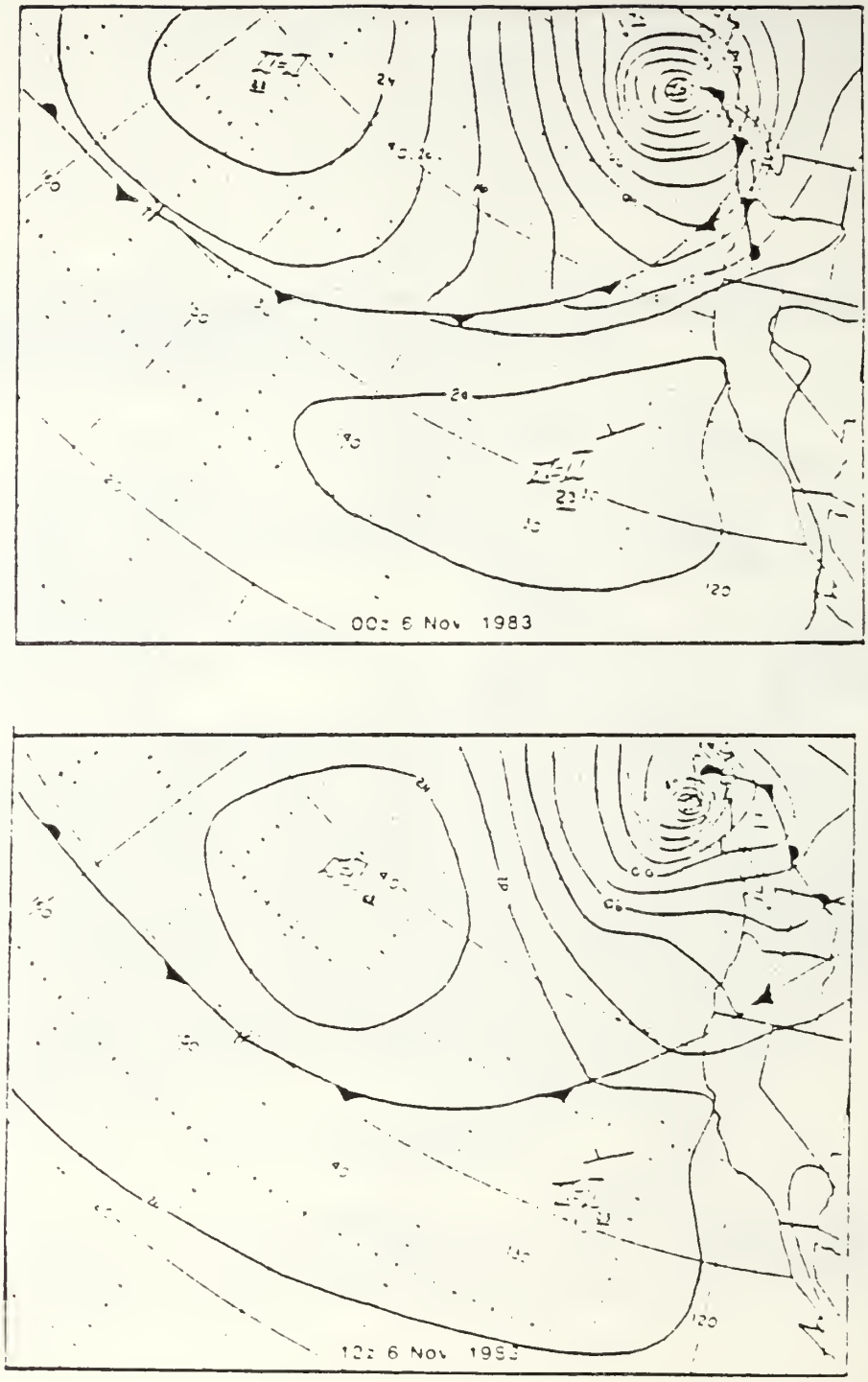

Fig. 3.26 6 November 1983 Surface Charts
a) 0000GMT (top), b) 1200GMT (bottom).

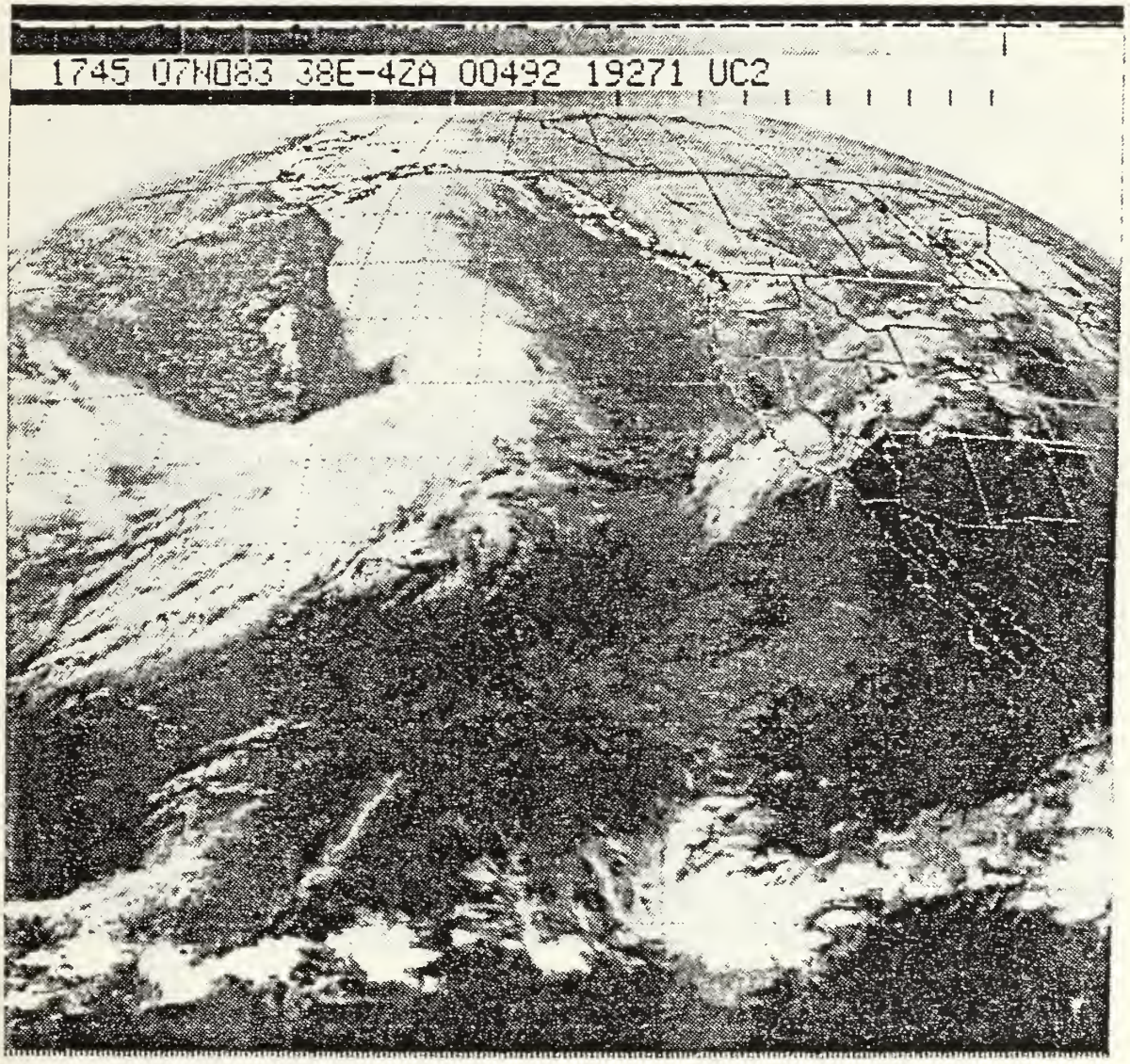

Fig. 3.27 7/1745GMT November 1983 Satellite Picture.

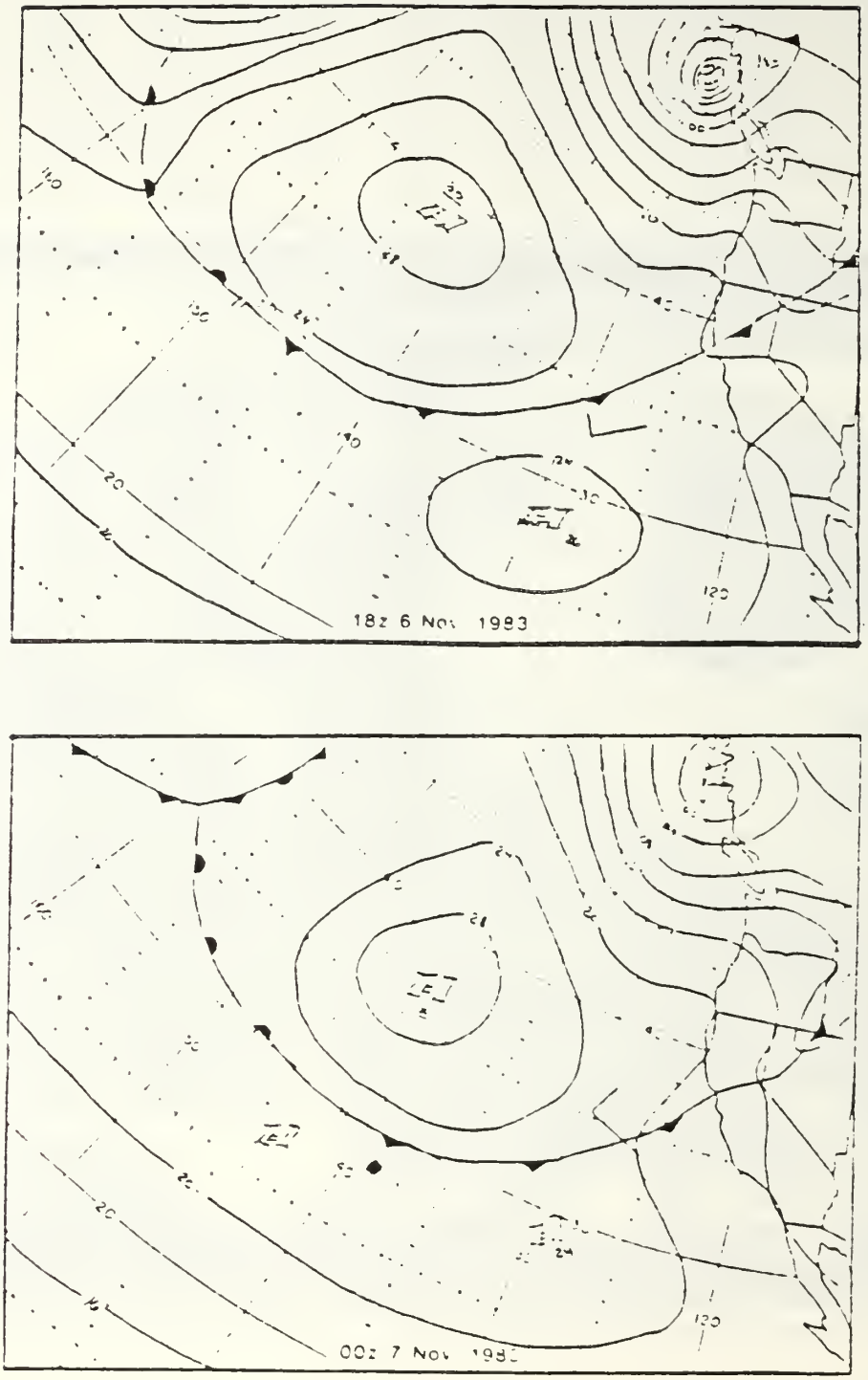

Fig. 3.28 6 - 7 November 1983 Surface Charts
a) 6/1800GMT (top), b) 7/0000GMT (bottom).

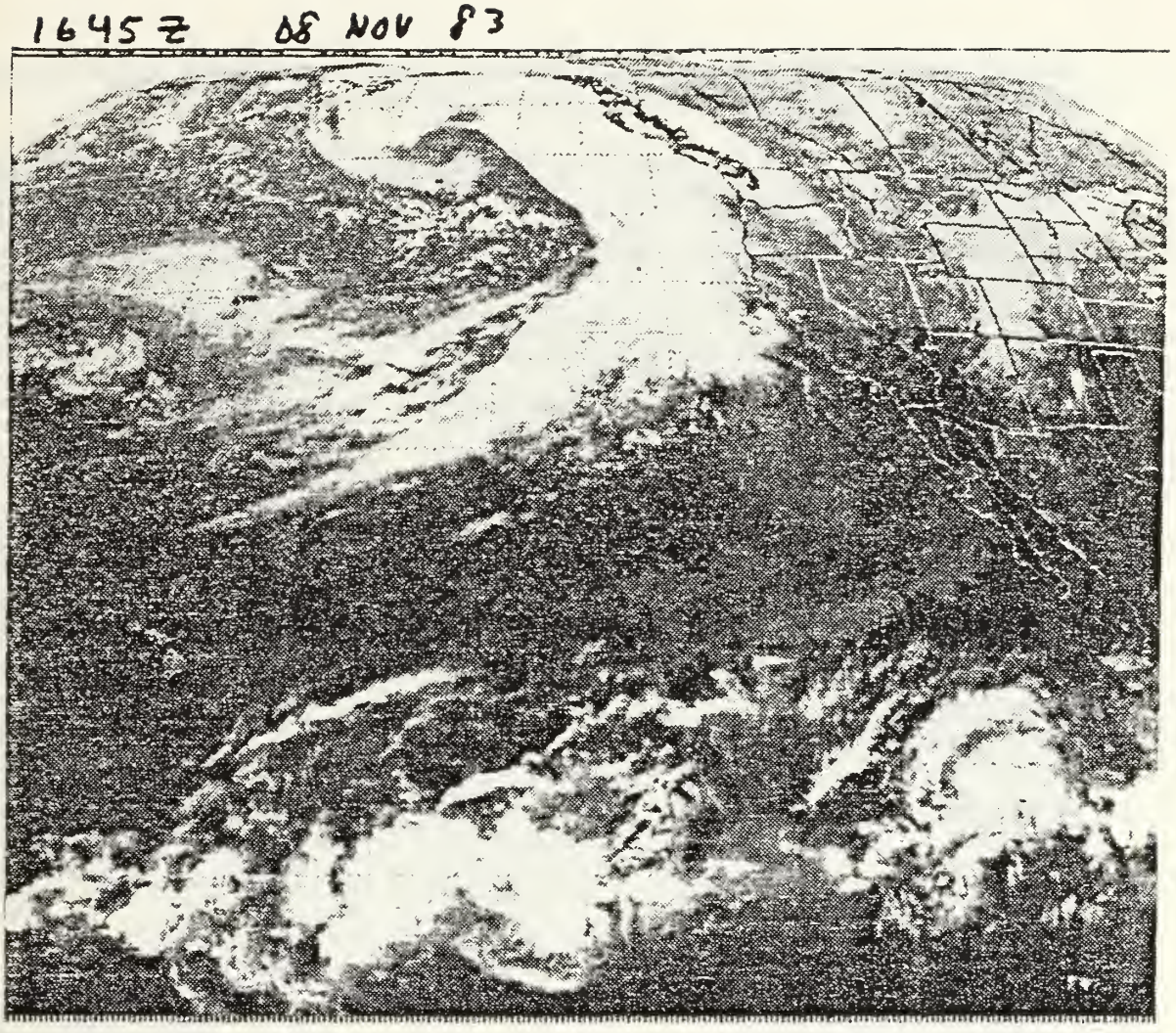

Fig. 3.29 8/1645GMT November 1983 Satellite Picture.

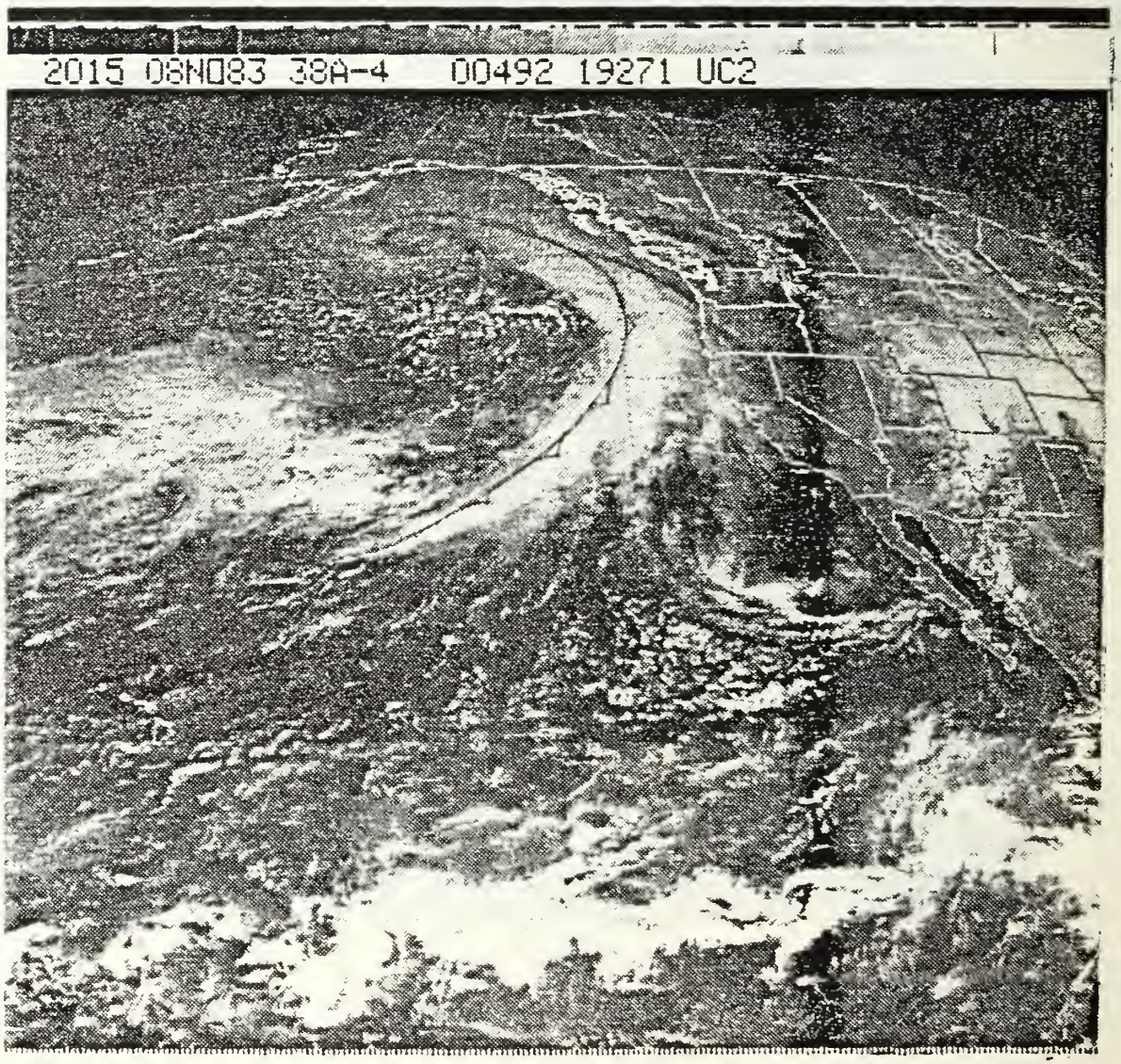

Fig. 3.30 8/2015 November 1983 Satellite Picture.

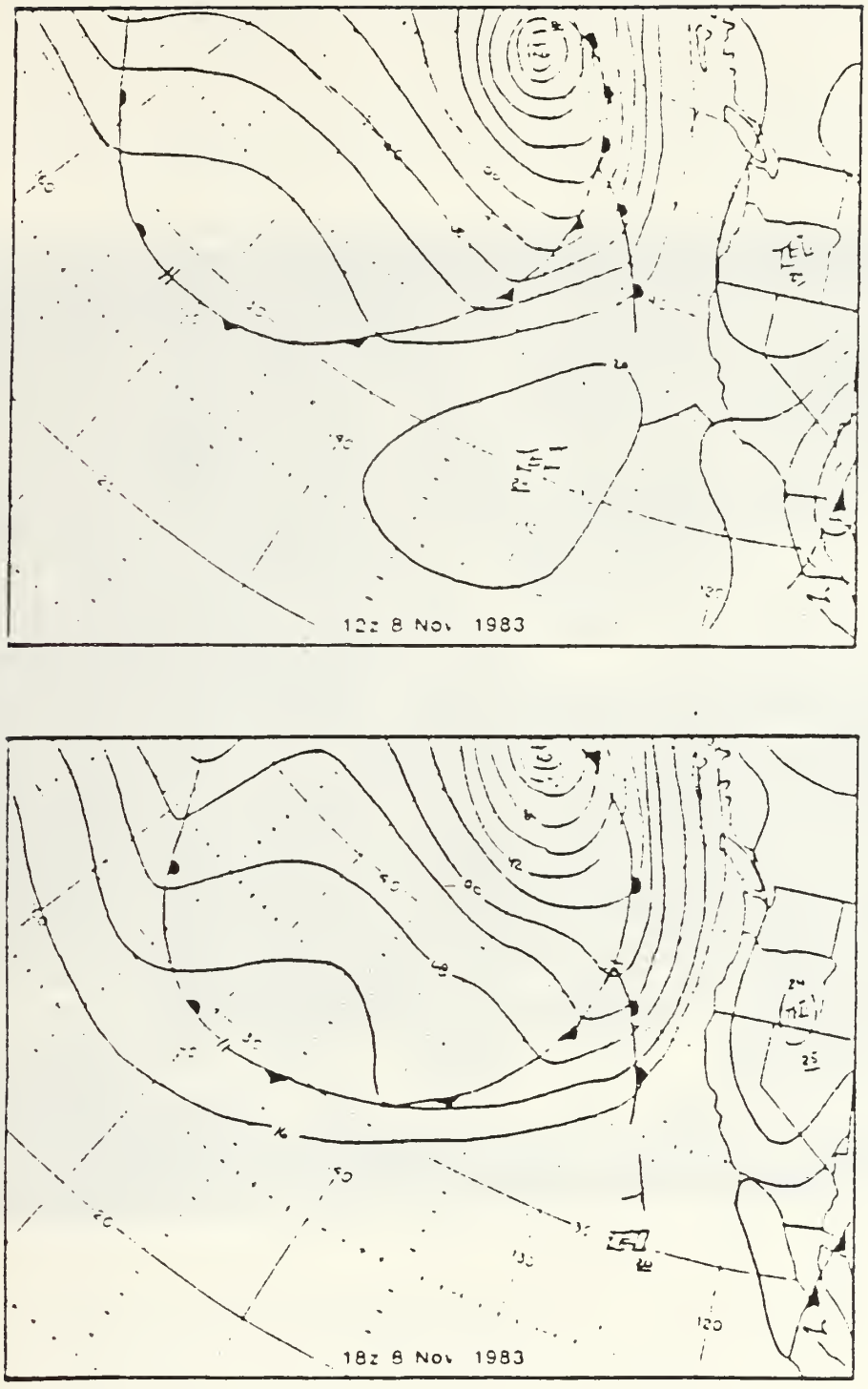

Fig. 3.31 8 November 1983 Surface Charts
a) 1200GMT (top), b) 1800GMT (bottom).

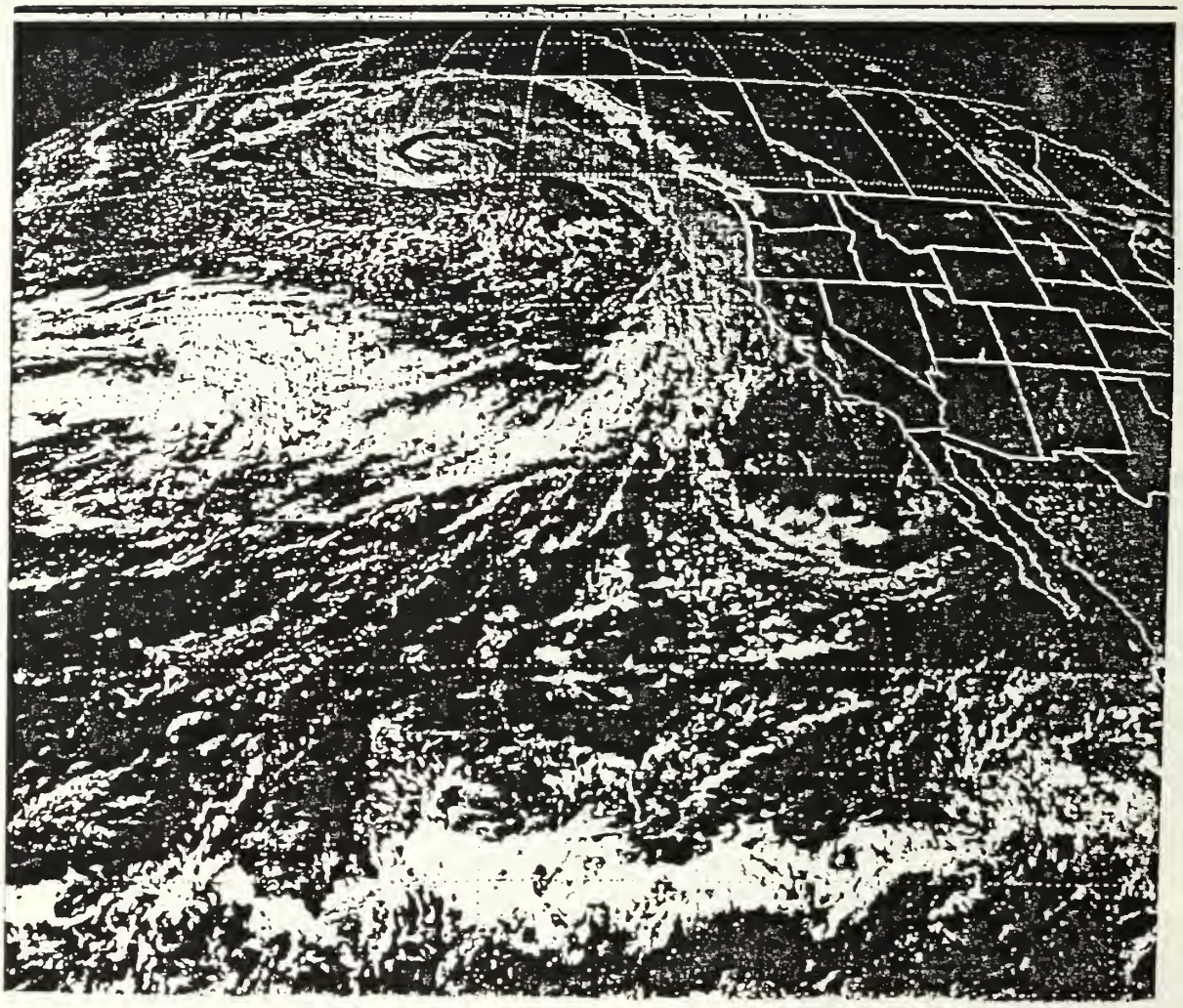

Fig. 3.32 8/2315GMT November 1983 Satellite Picture.

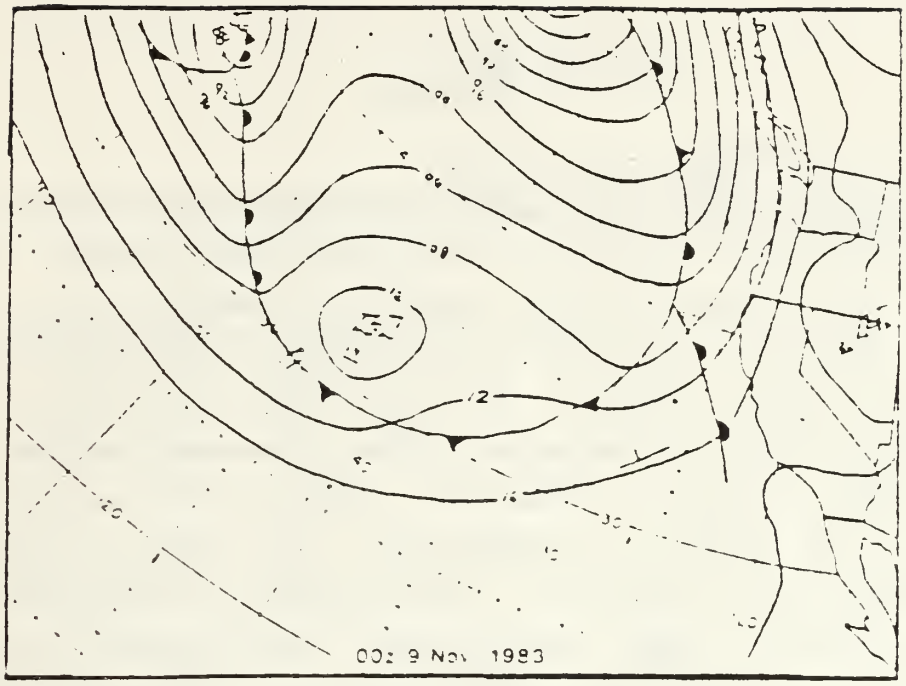

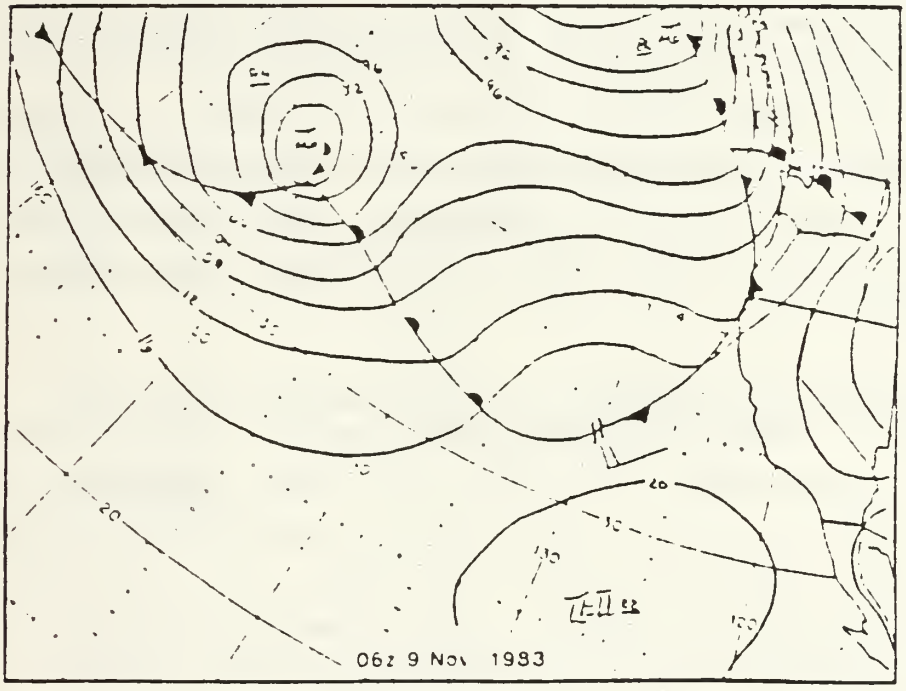

Fig. 3.33 9 November 1983 Surface Charts
a) 0000GMT (top), b) 0600GMT (bottom).

IV. RESULTS

A. MODEL APPLICATION

Thirty-six MILDEX radiosonde soundings were examined for possible radiation diagnosis using the MABL model. Those examined were based on the potential temperature and the specific humidity profiles (see sample output Fig. 4.1). All cases with a distinct humidity inversion were further examined relative to radiation. The inversion height, the mixed layer values of potential temperature and specific humidity, the potential temperature and specific humidity jumps across the inversion, the potential temperature and specific humidity lapse rates above the inversion, and the LCL were calculated from the profiles. These calculated values were used for a diagnosis of radiation. Also used were the Julian day, time of radiosonde launch, latitude, surface pressure and sea-surface temperature.

In this study, the interest was on how an integrated model using a simplified radiation scheme diagnosed radiation at a specific time. Therefore, only results from the first time step in the model calculations were used in the evaluation.

B. EXPLANATION OF TABLE I

Table I contains model and observed results for the selected soundings. FL refers to the radiosonde launch number. Of 36 launches, only the 17 listed had the features meeting the mixed layer model (see Fig 2.1). The date is in Pacific Standard Time (PST). Net incoming shortwave and net outgoing longwave radiations measured at the surface are in watts per meter squared. Measurement errors (uncertainties) for shortwave values are estimated to be 3% or nominally ±2 W/m^2 from 15 to 60 W/m^2 and ±10 W/m^2 for midday values around

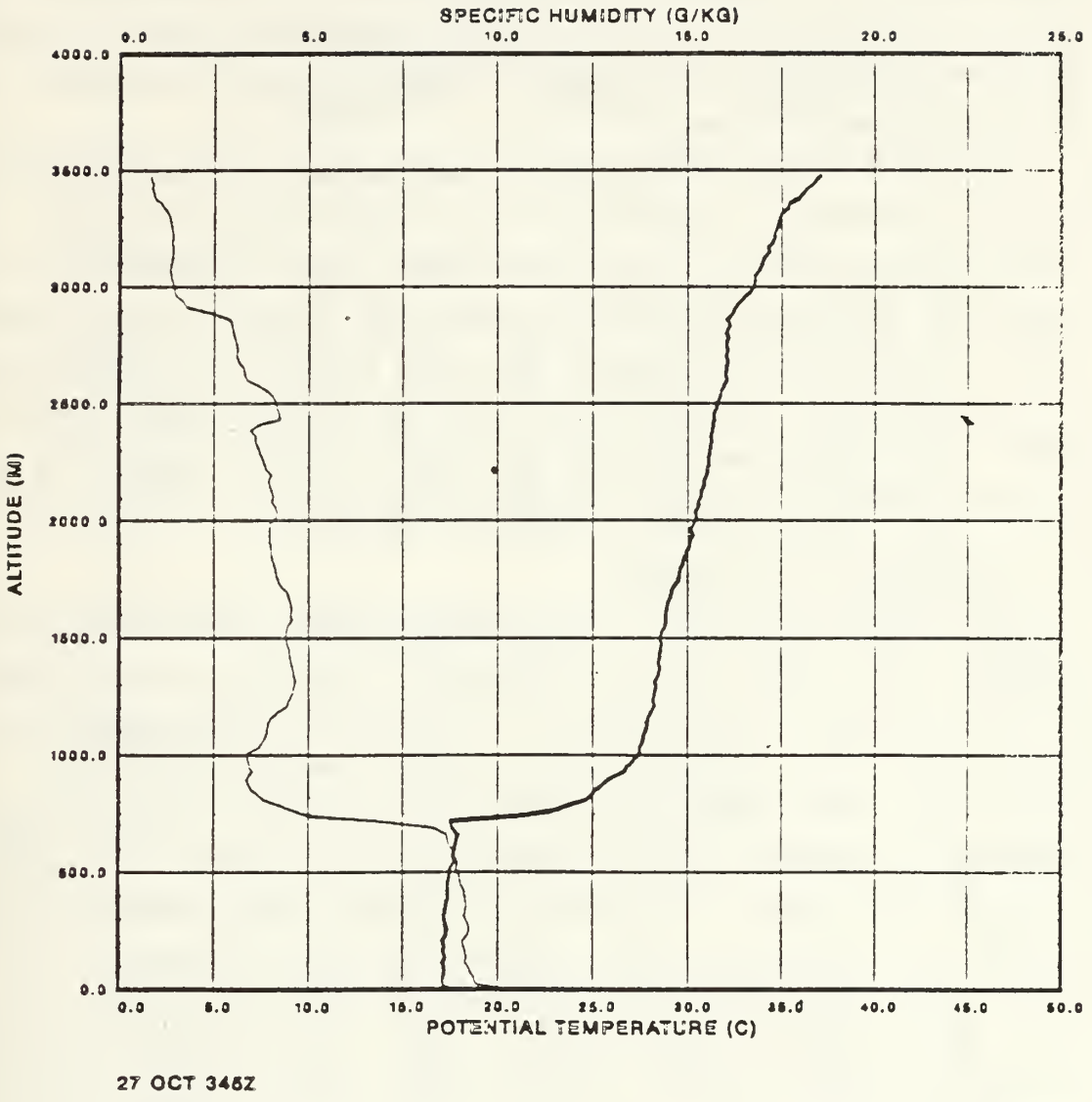

Fig. 4.1 Sample Model Potential Temperature and Specific Humidity Profiles - valid 27/0345Z.

300 W/m^2. Measurement error and surface estimated error for longwave values are ±15 W/m^2 (personal conversation, K. Katsaros, Atmospheric Science Department, University of Washington at Seattle). Clouds types are abbreviated and are in tens of % (i.e. 2 cu is 20% cumulus). N/C in the FL 29 shortwave radiation column refers to not considered due to measurement error.

The model clouds in table I are based on model diagnosis of the presence or absence of a cloud within the PBL. The model uses the LCL as the cloud base, and computes the cloud depth by subtracting the LCL from the height of the inversion. If the LCL is higher than the inversion, there are no clouds in the boundary layer, and the cloud depth is set to zero. The observed clouds in table I were based on both in-situ observations and satellite imagery.

C. DISCUSSION OF RESULTS

In this section, the similarities and differences between the model and the observed results are discussed. On the morning of October 26, a high pressure system dominated, and the observed sky was 20% cumulus (see Figs. 3.4 and 3.5). The model LCL was 157 m below the inversion, leading to a model cloud that was 157 m thick. The model cloud cover was, of course, overcast and extended from horizon to horizon. The model shortwave radiation (60.2 W/m^2) from 10/26/0800 was 20% greater than the hourly averaged measurement (50.3 W/m^2). This discrepancy occurred around sunrise when the solar angle was low, and accurate measurements are difficult and time sensitive. Additionally, the observed values were an hourly average which includes values taken before and after 0800 PST. The model outgoing (net) longwave radiation (36.6 W/m^2) was less than the observed value (71.8 w/m^2). The model diagnosed a relatively thick (157 m) overcast. Clouds emit longwave radiation back to earth. Hence the absence of observed

TABLE I

MODEL RESULTS

FL	DATE(PST)	RADIATION (Wm^{-2}) SHORTWAVE MODEL	SHORTWAVE OBSVD	LONGWAVE MODEL	LONGWAVE OBSVD	CLOUD DEPTH/TYPE MODEL	CLOUD DEPTH/TYPE OBSVD
	OCTOBER						
1	26/0800	60.2	50.3	36.6	71.8	157m	2 cu
2	26/2100	0.0	0.0	37.2	37.8	170m	10 sc
4	27/1700	56.9	55.4	191.2	29.7	0m	10 sc
5	28/0630	0.0	0.0	63.9	23.0	74m	10 st
6	28/1730	32.3	28.0	108.2	25.8	38m	7 cc 5 ac 6 cu
7	29/1700	55.4	85.6	182.9	55.9	0m	1 cu upper clds
	NOVEMBER						
16	1/0530	0.0	0.0	197.6	44.9	0m	5 cc
22	3/1730	23.4	26.9	141.9	9.2	39m	10 st
26	5/0930	391.0	305.0	226.7	77.5	28m	3 st 6 ci
27	5/1730	35.8	55.7	184.7	70.0	0m	2 ci
28	6/0330	0.0	0.0	31.9	46.6	233m	4 cc
29	6/1100	N/C	N/C	35.9	47.6	328m	1 cu
30	6/1730	28.4	41.8	173.3	8.2	0m	10 cu
33	8/0500	0.0	0.0	71.1	99.8	164m	2 st
34	8/1200	273.5	369.0	75.2	67.2	177m	9.5 sc
35	8/1730	16.3	12.4	158.1	35.3	40m	10 sc
36	8/2130	0.0	0.0	161.8	22.4	0m	10 cc

clouds caused the larger observed net longwave radiation to space.

Later that night (10/26/2100), the high still dominated (see Fig. 3.7) but the sky became overcast (100% sc). The model diagnosed a thick cloud (170 m), and since the observed cloud condition was overcast, the longwave radiation values were nearly equal (model: 37.2 , obsvd: 37.8 W/m^2). Since 2100 PST was well after sunset, short wave radiation was not considered.

The high remained the dominant synoptic feature for the next period (10/27/1700) (see Fig. 3.11a). The observed cloud condition was overcast (100% sc) but the satellite picture (see Fig. 3.8) showed breaks in the overcast. The short wave radiation value diagnosed by the model (56.9 W/m^2) was almost equal to the measured value (55.4 W/m^2). This is a surprising result since the model diagnosed no clouds, and the observed stratocumulus deck was completely overcast. This period is just before sunset, so the zenith angle of the sun was low. It is unknown if the horizon was actually clear, which would have explained the model's good performance. The longwave diagnosed value (191.2 W/m^2) was over six times the measured value (29.7 W/m^2). The difference is due to the fact that the observed clouds emitted longwave radiation back to earth and decreased the observed net longwave radiation.

Through the next period (10/28/0630) stratus cloud coverage existed (see Fig. 3.9) and the high pressure system was still still the dominant synoptic feature (see Fig. 3.12). Since this time was before sunrise, shortwave radiation was not considered. The model diagnosed a thin cloud (74 m), which emitted longwave radiation back to the surface, but not as much as the observed full dense stratus deck. Therefore the model overestimated the net longwave radiation (63.9 vs 23.0 W/m^2).

Later on the 28th (1730), the model still underestimated cloud coverage. A broken (60%) lower layer of cumulus was observed in addition to high clouds (see Fig. 3.13). The high began to weaken as the warm sector ahead of a cold front approached (see Fig. 3.14a). The model diagnosed LCL was close to the inversion (38 m below), so a thin cloud was estimated. The high clouds emitted more longwave radiation back to the surface than did the model's environment of no clouds above the boundary layer (model: 108.2, obsvd: 25.8 W/m^2). The model's shortwave diagnosis (32.3 W/m^2) was consistent with the observed value (28.0 W/m^2) since the model diagnosed a thin cloud and broken clouds were observed. The concern with this case is the agreement in the shortwave radiation values but large disagreement in the longwave values results. Perhaps, the shortwave radiation agreement exists because of a low sun angle.

For the next time period (10/29/1700), the cold front remained west of the experimental region (see Fig. 3.15a). Observed cloud cover was scattered cumulus and stratocumulus clouds. Although the model diagnosed no clouds, the model still underestimated the measured shortwave radiation (model: 55.4; obsvd: 85.6 W/m^2). This period is near sunset, a time not optimal for testing of the model. Observed upper clouds in addition to scattered cumulus emitted longwave radiation which, caused the model (182.9 W/m^2) to overestimate the net longwave radiation observed (55.9 W/m^2).

The next period (11/1/0530) coincided with a frontal passage (see Fig. 3.18a). Cloud cover increased (see Fig. 3.17) and was accompanied with rain, showers and drizzle. The valid time was before sunrise, thus shortwave radiation was not considered. The model again failed to predict any clouds, however clouds were observed above the boundary layer (50% cc). Therefore, the model, without upper clouds, overestimated the net longwave radiative flux (197.6 vs 44.9 W/m^2).

The subtropical high was re-established on 11/3/1730 over the MILDEX area (see Fig. 3.23a). An overcast stratus deck was observed (see Fig. 3.20). The time was near sunset (1730) and the model's shortwave diagnosis (23.4 W/m^2) agreed with the observed value (26.9 W/m^2) since the model diagnosed a cloud and stratus clouds were observed. The model LCL was 39 m below the inversion, producing a relatively thin cloud. The observed stratus deck emitted more longwave radiation than the 39 m diagnosed cloud, so the model overestimated the net longwave radiation (141.9 vs 9.2 W/m^2).

A high pressure system continued to dominate the next period (11/5/0930) examined (see Fig. 3.25b). Scattered stratus and broken cirrus were observed and the model diagnosed the occurrence of thin boundary layer clouds (28 m) correctly. The model diagnosed the highest value (391 W/m^2) of shortwave radiation in this data set, and the measured value was also one of the highest (305 W/m^2). The broken cirrus clouds reduced the incoming solar radiation, causing a higher model diagnosed value than what was actually measured. This case (FL26) was similar to other cases (.e.g. FL's 5, 6, 22, and 35), in which the LCL was close to but below the inversion. However, high clouds were observed and presumably, these high clouds and the scattered stratus clouds emitted more longwave radiation to the surface than did the thin diagnosed boundary layer cloud. Thus, the model's net longwave emittance was larger (model: 226.7, obsvd: 77.5 W/m^2).

A weak cold front to the west dissipated, and had little effect on the synoptic conditions during the next period (11/5/1730) (see Fig 3.26a) examined. Scattered cirrus clouds were the only clouds observed and, as with other cases (e.g. FL's 4, 7, 16, 30 and 36), the LCL was diagnosed above the inversion for FL 27. However, the observed high

clouds emitted longwave radiation back to the surface. Thus, the model's clear sky had a larger net longwave radiation value (model: 184.7, obsvd: 70 W/m^2). The model's sunset diagnosis of shortwave radiation (35.8 W/m^2) was again smaller than the measured value (55.7 W/m^2) because of the diagnosed and observed cloud differences.

The warm sector ahead of the next approaching cold front began to influence synoptic conditions during the next periods (11/6/0330 and 11/6/1100) (see Figs. 3.26b and 3.28a). Cloud cover was observed as scattered to broken cumulus throughout the day. FL 28 was a morning launch so shortwave radiation was not considered. The model diagnosed a low LCL for both periods in the morning of November 6 (11/6/0330 and 11/6/1100), resulting in thick clouds (233m and 328m, respectively). During both periods, scattered cumulus (less than 40%) were observed. In both cases, the model underestimated the net outward longwave radiation (31.9 vs 46.6, and 35.9 vs 47.6 W/m^2, respectively). Since the model diagnosed thick clouds extended from horizon to horizon, the model results indicated more longwave radiation emittance back to the surface than that emitted from the observed cumulus.

The next period (11/6/1730) coincided with a frontal passage (see Fig. 3.28b). The observed sky was overcast cumulus, but the model diagnosed no clouds. As in previous cases (e.g. FL's 4, 7, 16, and 27), the model overestimated the net longwave radiation emitted (model: 173.3; obsvd: 8.2 W/m^2). This period was again near sunset, so the model's shortwave radiation diagnosis (28.4 W/m^2) was not in agreement with the measured shortwave radiation (41.8 W/m^2).

During the next period (11/8/0500), an intense low pressure system was located to the north in the Gulf of Alaska, but a weakening high was still the dominant synoptic feature in the MILDEX region (see Fig. 3.31a). Stratus clouds were

observed (see Fig. 3.29). As with previous cases (e.g. FL's 1, 28, and 29), the model diagnosed a thick cloud (164 m) for FL 33, while the observation was only scattered (20% st), therefore the model underestimated net longwave emittance (71.1 vs 99.8 W/m^2). The launch was well before sunrise, thus shortwave radiation was not considered.

Cloud cover increased and became overcast over the next period (11/8/1200), (see Fig. 3.30). The high dissipated, as the warm front moved into the region (see Fig. 3.31b). The model diagnosed LCL was 177 meters below the diagnosed inversion. As was the case with FL 2, the model value (75.2 W/m^2) agreed closely with the observed value (67.2 W/m^2), slightly overpredicting the longwave emittance. This noon launch time produced the highest measured value of shortwave radiation (369.0 W/m^2) received. The model value (273.5 W/m^2) was lower since the model diagnosed a thick horizon to horizon cloud, while the observed cloud cover had breaks in the overcast.

During the next period (11/8/1730), the MILDEX region was in the warm sector of an approaching cold front (see Fig. 3.33a). Cloud cover was overcast (100% sc) (see Fig. 3.32). The model diagnosed a thin cloud (40m). As in previous cases (e.g. FL' 5, 6, 22, and 26) in which thin clouds were diagnosed but broken to overcast clouds were observed, the model overestimated the net longwave radiation (158.1 vs 35.3 W/m^2). This period was again near sunset, so the model's shortwave radiation diagnosis (16.3 W/m^2), although close to the measured shortwave radiation (12.4 W/m^2), was not of significance.

The final period (11/8/2130) considered was prior to the final frontal passage of the MILDEX experiment (see Fig. 3.33). Cloud cover was overcast (see Fig. 3.32). The last launch (FL 36) was at night, therefore shortwave radiation was not considered. This case is similar to previous cases

(e.g. FL's 4, 7, 16, 27, and 30) when no clouds were diagnosed, but upper clouds were observed (100% cc), therefore the model greatly overestimated the net longwave radiation emitted (161.8 vs 22.4 W/m^2).

V. CONCLUSIONS

Over long periods of time, energy absorbed (shortwave radiation) by the MABL is approximately equal to energy emitted (longwave radiation), but predicting the perturbations in radiative flux is important in the evolution of the MABL. The perturbations of boundary layer parameters such as temperature and humidity can change in a matter of hours, thus affecting and being affected by radiation flux.

A. SHORTWAVE SUMMARY

The model calculated shortwave radiation values from solar angle and MABL parameters. At night, shortwave radiation was not considered (e.g. FL's 2, 5, 16, 28, 33, and 36). Discrepancies occurred near sunrise (.e.g. FL 1) and sunset (e.g. FL's 7, 27, and 30). The reasons for these discrepancies could be threefold. First, did the model use the proper solar angle to get its shortwave radiation value when the solar zenith angle is most critical? Second, was the boundary layer cloud cover at the horizon truly representative of the actual cloud cover? Third, the measured values were an hourly average. Near sunset/sunrise values were based on measurements both before, which gave a nonzero/zero contribution, and after which gave a zero/nonzero value. Thus, model runs near sunrise and sunset were not good for evaluating the shortwave calculations of the model.

For FL 26, the model overestimated the observed shortwave value due to cirrus clouds above the model's environment. The model (e.g. FL 34) underestimated the shortwave radiation when a thick horizon to horizon cloud was diagnosed by the model and the observed sky conditions indicated breaks in the overcast. However, over one half of the model's daytime estimations were within 20 W/m^2 of the measured shortwave value (e.g. FL's 4, 6, 22, 27, 30, and 35).

Another reason for errors was the simple radiation scheme used by the model. Water vapor absorption beyond 1.7 μm was ignored despite the fact that a major absorption band exists at 1.87 μm. Also, the shortwave calculation with clouds was restricted to the region between the LCL and the inversion. In the cloudy case, the layer below the cloud base was assumed to emit zero shortwave radiation flux, despite the presence of aerosols.

B. LONGWAVE SUMMARY

When thick clouds were diagnosed and broken or overcast conditions were observed, the model was within 15% of the measured value (e.g. FL's 2, and 34). When either no clouds or thin clouds were diagnosed, and clouds were observed, the model greatly overestimated the net longwave radiation emitted (e.g. FL's 4, 5, 6, 7, 16, 22, 26, 27, 30, 35, and 36). The model is deficient in that it only diagnoses clouds in the boundary layer.

When a thick cloud (cases with a model cloud greater than 157 m) was diagnosed, and the observed sky was scattered (20% or less), the model underestimated the longwave radiation emitted (FL's 1, 28, 29 and 33). The diagnosed thick clouds emitted more longwave radiation back to the surface than the observed scattered clouds emitted downward.

C. RECOMMENDATIONS

These recommendations pertain to specifications within the model and to procedures for evaluating it with in-situ data. Since the model provides a point estimate, clouds are either there or not there (100% or 0%). When clouds are diagnosed they extend from horizon to horizon. Partial cloud cover certainly has to be considered for both shortwave and longwave radiation effects on the Boundary Layer. A statistical approach for percentage cloud cover could, perhaps, be included for more realistic cloud effects.

Improving parametization is necessary for determining the LCL. This is important because the height of the LCL determines the cloud thickness. Further development of mixed layer gradients within the model is necessary.

The model does not consider clouds above the mixed layer and that is a severe limitation. The PBL is not self-deterministic, but rather dependent on larger scale external factors, such as the radiative effects of upper level clouds.

Many MILDEX radiosondes were launched to coincide with satellite passes, and as a result, radiosondes were launched near 0000Z and 1200Z, which corresponds to 0700 PST and 1900 PST. Solar shortwave radiation values should be evaluated at local noon when the shortwave values are at their greatest and the solar angle is least critical. Therefore, it is recommended that future radiation data-gathering experiments include radiosonde launches close to local noon.

The model is a potentially powerful tool but still has limitations. Currently, the model is best used for explaining dynamical processes of the boundary layer rather than radiative processes. Further research and development of the model is needed with the eventual goal of an operational boundary layer model.

LIST OF REFERENCES

Andre, J. C., and L. Mahrt, 1982: The nocturnal surface inversion and influence of clear-air radiative cooling. *J. Atmos. Sci.*, 39, 864-878.

Beniston, M., and J. Schmetz, 1985: A three-dimensional study of Mesoscale model response to radiative forcing. *Boundary Layer Met.*, 31, 149-175.

Boyle, P. J., Davidson, K. L., and G. E. Schacher, 1984: Evaluation of an integrated mixed-layer model for single station prediction in a Marine Regime. Preprints Proc Nowcasting-II Symposium, Norrkoping, Sweden, ESA SP-208, 323-327.

Businger, J. A., J. C. Wyngaard, Y. Izumi, and E .F. Bradley, 1971: Flux profile relationships in the atmospheric surface layer. *J. Atmos. Sci.*, 28, 181-189.

Davidson, K. L., C. W. Fairall, P. J. Boyle, and G. E. Schacher, 1984: Verification of an atmospheric mixed-layer model for a coastal region. *J. Clim. Appl. Meteor.*, 23, 617-636.

Davidson, K. L., and R. W. Garwood, 1984: Coupled oceanic and atmospheric mixed layer model. *Dynamics of Atmospheres and Oceans*, 8, 283-296.

Deardorff, J. W., 1976: On the entrainment rate of a stratocumulus-topped Mixed layer. *Quart. J. R. Met. Soc.*, 102, 563-582.

Deirmendjian, D., 1969: *Electromagnetic Scattering on Spherical Polydispersions*, American Elsevier, New York, 290 pp. 102, 563-582.

Fairall, C. W., K. L. Davidson, and G. E. Schacher, 1981: A review and evaluation of integrated atmospheric boundary-layer models for maritime applications. *NPS-63-81-004*, Naval Postgraduate School, Monterey, Ca., 89 pp.

Fairall, C. W., K. L. Davidson, and G. E. Schacher, 1983: An analysis of the surface production of sea-salt aerosols. *Tellus*, 35B, 31-39.

Fairall, C. W., and K. L. Davidson, 1986: Dynamics and Modeling of aerosols in the Marine Atmospheric Boundary Layer. *Whitecaps and Air/Sea Interaction*, E. C. Monahan, and G. MacNiocaill, Ed., D. Reidel.

Fleagle, R. G., and J. A. Businger, 1980: *An Introduction to Atmospheric Physics, 2nd ed.*, Academic Press, 432 pp.

Hale, G. M., and M. R. Querry,1973: Optical constants of water in the 200nm-200μm wavelength range. *Appl. Opt.*, 12, 555-563.

Joseph, J. W., W. J. Wiscombe, and J. A. Weinman, 1976: The Delta-Eddington approximation for radiative flux transfer, *J. Atmos. Sci.*, 33, 2452-2459.

Lacis, A., A., and J. E. Hansen, 1974: Parametization fro the Absorption of solar radiation in the Earth's atmosphere. *J. Atmos. Sci.*, 31, 118-133.

Liou, K., 1980: *An Introduction to Atmospheric Radiation.*, Academic Press, 392 pp.

Schacher, G. E., K. L. Davidson, T. Houlihan, and C. W. Fairall, 1981 Measurements of the rate of dissipation of turbulent kinetic energy over the ocean. *Boundary Layer Met.*, 20, 321-333.

Selby, J. E. A., E. P. Shettle, and R. A. McClatchey, 1976: Atmospheric transmittance from 0.25 to 28.5 μm: Supplement LOWTRAN 3B. Tech. Rep. AFGL-TR-76-0258, Air Force Geophysics Laboratory Hanscom AFB, MA, 79 pp.

Slingo, A., R. Brown, and C. L. Wrench, 1982: A field study of nocturnal stratocumulus: III. High resolution radiative and microphysical observations, *Quart. J. R. Met. Soc.*, 108, 145-166.

Slingo, A., and H. M. Schrecker, 1982: On the short-wave radiative properties of stratiform water clouds. *Quart. J. R. Met. Soc.*, 108, 407-426.

Smithsonian Meteorological Tables, 1963: Sixth Ed., Smithsonian Institution, 527 pp.

Stage, S. A., 1979: A model of modification of the cloud-topped marine boundary layer during cold air outbreaks. PH.D. thesis, University of Washington, 281 pp.

Stage,S. A., and J. A. Businger, 1981: A model for entrainment into a cloud-topped marine boundary layer. *J. Atmos. Sci.*, 38, 2213-2242.

INITIAL DISTRIBUTION LIST

No.		Copies
1.	Defense Technical Information Center Cameron Station Alexandria, VA 22304-6145	2
2.	Library, Code 0142 Naval Postgraduate School Monterey, CA 93943-5000	2
3.	Chairman, Code 63Rd Department of Meteorology Naval Postgraduate School Monterey, CA 93943-5000	1
4.	Chairman, Code 68Mr Department of Oceanography Naval Postgraduate School Monterey, CA 93943-5000	1
5.	Professor K. L. Davidson, Code 63Ds Department of Meteorology Naval Postgraduate School Monterey, CA 93943-5000	5
6.	Professor R. W. Garwood, Code 68Gd Department of Oceanography Naval Postgraduate School Monterey, CA 93943-5000	1
7.	Professor P. A. Durkee, Code 63De Department of Meteorology Naval Postgraduate School Monterey, CA 93943-5000	1
8.	P. J. Boyle, Code 63Bp Department of Meteorology Naval Postgraduate School Monterey, CA 93943-5000	1
9.	Professor G. E. Schacher, Code 63Sq Department of Physics Naval Postgraduate School Monterey, CA 93943-5000	1
10.	Captain Steven B. Dreksler Det 1, 1WW (MAC) BOX 20 FPO, San Francisco, CA 96630-5000	2
11.	Director Naval Oceanography Division Naval Observatory 34th and Massachusetts Avenue NW Washington, DC 20390	1
12.	Commander Naval Oceanography Command NSTL Station Bay St. Louis, MS 39522	1

13. Commanding Officer 1
Naval Oceanographic Office
NSTL Station
Bay St. Louis, MS 39522

14. Commanding Officer 1
Fleet Numerical Oceanography Center
Monterey, CA 93943-5005

15. Commanding Officer 1
Naval Ocean Research and Development Activity
NSTL Station
Bay St. Louis, MS 39522

16. Commanding Officer 1
Naval Environmental Prediction Research Facility
Monterey, CA 93943-5006

17. Chairman, Oceanography Department 1
U.S. Naval Academy
Annapolis, MD 21402

18. Ms. Julie Haggerty 1
Naval Environmental Prediction Research Facility
Monterey, CA 93943-5006

19. Dr. Thomas Spence, Code 1122 1
Physical Oceanography
800 N. Quincy Street
Arlington, VA 22217

20. AFIT/CIRF 1
Wright-Patterson AFB
OH 45433

21. USAFETAC/TS 1
Scott AFB
IL 62225

22. AFGWC/TS 1
Offutt AFB
NE 68113

23. Captain Steven B. Dreksler 1
NOCC/JTWC
BOX 12
FPO, San Francisco, CA 96630-5000

DUDLEY KNOX LIBRARY
NAVAL POSTGRADUATE SCHOOL
MONTEREY, CALIFORNIA 93943-5002

219247

Thesis
D735 Dreksler
c.1 An examination of radiation in an integrated marine atmospheric boundary layer model.

219247

Thesis
D735 Dreksler
c.1 An examination of radiation in an integrated marine atmospheric boundary layer model.

thesD735
An examination of radiation in an integr
3 2768 000 67189 5
DUDLEY KNOX LIBRARY